Influence of deformation and fluids on Ar retention in white mica: Dating the Dover Fault, Newfoundland Appalachians

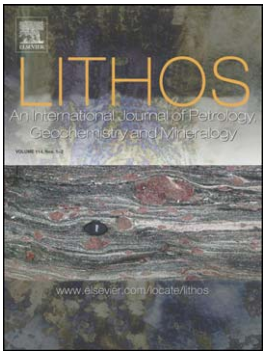

Influence of deformation and fluids on Ar retention in white mica: Dating the Dover Fault, Newfoundland Appalachians

Dawn A. Kellett, Clare Warren, Kyle Larson, Horst Zwingmann, Cees R. van Staal, Neil Rogers

PII: S0024-4937(16)00109-2
DOI: doi: 10.1016/j.lithos.2016.03.003
Reference: LITHOS 3862

To appear in: *LITHOS*

Received date: 21 October 2015
Accepted date: 4 March 2016

Please cite this article as: Kellett, Dawn A., Warren, Clare, Larson, Kyle, Zwingmann, Horst, van Staal, Cees R., Rogers, Neil, Influence of deformation and fluids on Ar retention in white mica: Dating the Dover Fault, Newfoundland Appalachians, *LITHOS* (2016), doi: 10.1016/j.lithos.2016.03.003

Influence of deformation and fluids on Ar retention in white mica: dating the Dover Fault, Newfoundland Appalachians

Dawn A. Kellett*[1], Clare Warren[2], Kyle Larson[3], Horst Zwingmann[4], Cees R. van Staal[5], Neil Rogers[1]

[1]*Geological Survey of Canada, 601 Booth St., Ottawa, ON, Canada, K1A 0E8*

[2]*Department of Earth and Environmental Sciences, CEPSAR, Open University, Milton Keynes, UK*

[3]*Earth and Environmental Sciences, University of British Columbia, Okanagan, FIP353-3247 University Way, Kelowna, BC, Canada, V1V 1V7*

[4]*CSIRO Energy Flagship, Bentley, WA 6102, Australia; present address Department of Geology and Mineralogy, Graduate School of Science, Kyoto University, Kitashirakawa Oiwakecho, Kyoto 606-8502, Japan*

[5]*Geological Survey of Canada, 1500-605 Robson St., Vancouver, BC, V6B 5J3, Canada*

*Corresponding author: dawn.kellett@canada.ca.

KEYWORDS

^{40}Ar/^{39}Ar geochronology; geochronology; shear zone; Appalachian orogen; fault reactivation; Ganderia; Salinic orogeny; Acadian orogeny; Neoacadian orogeny

HIGHLIGHTS

1. Low temperature deformation and fluid events redistribute ^{40}Ar in white mica.
2. Dating the timing of deformation recorded by white mica requires *in situ* analysis.

3. Salinic D_2 deformation in Newfoundland Ganderia occurred ca. 422 Ma.
4. Sinistral slip at Ganderia-Avalonia boundary between 422-405 Ma, dextral reactivation ca. 385 Ma.
5. Brittle slip persisted until at least Mississippian.

ABSTRACT

White mica $^{40}Ar/^{39}Ar$ analyses may provide useful constraints on the timing of tectonic processes, but complex geological and thermal histories can perturb Ar systematics in a variety of ways. Ductile shear zones represent excellent case studies for exploring the link(s) between dynamic re-/neo-crystallization of white mica and coeval enhanced fluid flow, and their effect on $^{40}Ar/^{39}Ar$ dates. White mica $^{40}Ar/^{39}Ar$ dates were collected from compositionally similar granites that record different episodes of deformation with proximity to the Dover Fault, a terrane-bounding strike-slip shear zone in the Appalachian orogen, Newfoundland, Canada. $^{40}Ar/^{39}Ar$ data were collected *in situ* by laser ablation and by step heating single crystals. Results were compared to each other and against complementary U-Pb zircon and monazite, and K-Ar fault gouge analysis.

Although step-heat $^{40}Ar/^{39}Ar$ is a widely applied method in orogenic settings, this dataset shows that relatively flat step-heat $^{40}Ar/^{39}Ar$ spectra are in contradiction with wide spreads in *in-situ* $^{40}Ar/^{39}Ar$ dates from the same samples, and that plateau dates in some cases yielded mixed dates of equivocal geological significance. This result indicates that the step-wise release of Ar from white mica likely homogenizes and obscures spatially-controlled Ar isotope reservoirs in white mica from sheared rocks. In contrast, *in situ* laser ablation $^{40}Ar/^{39}Ar$ analysis preserves the spatial resolution of ^{40}Ar reservoirs that have been variably reset by deformation and fluid

interaction. This study therefore suggests that laser ablation is the best method for dating the timing of deformation recorded by white mica. Final interpretation of results should be guided by microstructural analysis, estimation of deformation temperature, chemical characterization of white mica, and complementary chronometers.

Overall the dataset shows that granitic protoliths were emplaced between 430-422 Ma (U-Pb zircon). High strain deformation along the Wing Pond Shear Zone occurred between ca. 422-405 Ma (U-Pb monazite and $^{40}Ar/^{39}Ar$). Subsequent patchy Ar loss in white mica occurred locally during low T shear (<400 C), and via post-deformation fluid interactions. Low-temperature reactivation of the Dover Fault, a narrow segment of the Wing Pond shear zone, occurred at ca. 385 Ma ($^{40}Ar/^{39}Ar$). K-Ar dating of authigenic illite in fault gouge from the broadly co-linear brittle Hermitage Bay Fault indicates that slip along the terrane boundary persisted until at least the Mississippian.

INTRODUCTION

The $^{40}Ar/^{39}Ar$ step heating method applied to white mica is a common and valuable tool for studying metamorphic rocks (e.g. Bröcker et al., 2013; McWilliams et al., 2013; Forster and Lister, 2014). The method of progressively releasing Ar from white mica crystals has been proposed to mimic diffusion of Ar in nature. The age patterns reflected by Ar release spectra are often interpreted as corresponding to Ar distribution in the crystal(s) such that the thermal history of the grain(s) can be recovered (e.g. Harrison et al., 2009; Kula and Spell, 2012). However, metamorphosed and deformed rocks often record complex geological and thermal histories. The thermal history may be in competition with other physical processes that influence final Ar distributions in white mica grains and consequently, step-heat release spectra can be difficult to

interpret or can yield equivocal results. For example, "inherited" Ar, relating to ^{40}Ar formed at an earlier time than the episode being dated, may persist in white mica if insufficient time was spent at temperatures that promote fast diffusion (in practice, well above its Ar closure temperature; Monié, 1990; Viete et al., 2011; Mottram et al., 2015). Moreover, white mica can grow during protracted low temperature metamorphism, at conditions for which thermal diffusion of Ar is inefficient (Reuter and Dallmeyer, 1989). Deformation can promote mica recrystallization or neocrystallization (Sherlock et al., 2003; Mulch and Cosca, 2004; Mulch et al., 2005), and can alter the effective white mica Ar diffusion distance (Kramar et al., 2001; Cosca et al., 2011). Finally, fluid infiltration, or lack thereof, can impact ^{40}Ar content in white mica, through the introduction of extraneous Ar, inefficient removal of radiogenic Ar, or by promoting mineral alteration (e.g. Warren et al., 2012a; review in Kelley, 2002). In situ and single grain fusion techniques can reveal complexities in the ^{40}Ar composition of white mica resulting from these processes that are otherwise obscured or homogenized in step heating experiments.

Ductile shear zones represent excellent case studies for exploring the link between dynamic re-/neo-crystallization of white mica and coeval enhanced fluid flow at a variety of temperatures. In this study we investigate the influence of deformation and fluids on Ar behavior in white mica from compositionally similar granites with different deformation patterns relating to the Dover Fault, a terrane-bounding strike-slip shear zone in the Appalachian orogen of Newfoundland, Canada. Detailed age information extracted from spatially-controlled *in-situ* ^{40}Ar/^{39}Ar analyses is compared to step-heat spectra obtained from single crystals separated from the same samples. ^{40}Ar/^{39}Ar data are bracketed by complementary U-Pb zircon and monazite age data, which record the timing of (re-)crystallization of those accessory phases. Brittle fault movement that formed a well-developed gouge within the Hermitage Bay fault zone is

constrained by dating of authigenic illite using the conventional K-Ar method (see Zwingmann and Mancktelow, 2004; Zwingmann et al., 2010) and confines the timing on the latest active retrograde deformation event along the terrane boundary. These data together demonstrate the value of high spatial resolution $^{40}Ar/^{39}Ar$ age data in elucidating the thermal and deformational histories of deformed and metamorphosed rocks. Furthermore, our data permit a time reconstruction of the deformation history of the Ganderian margin during the Salinic, Acadian and Neoacadian orogenies by direct dating of fault rocks.

GEOLOGICAL FRAMEWORK

The Appalachian-Caledonian orogenic system exposed in eastern North America, eastern Greenland, Scandinavia and central Europe records the Paleozoic, progressive closures of the Iapetus, Tornquist and Rheic oceans, and associated episodic accretionary events that culminated in the formation of the Pangaea supercontinent (van Staal et al., 1998; 2009). Within the eastern Canada Appalachians, accretion of the Dashwoods, Ganderia, Avalonia and Meguma terranes (and associated arcs, back-arcs and oceanic fragments) was accompanied by progressively eastward shifts (in present day coordinates) of orogenic deformation, metamorphism and magmatism, identified as the Taconic (495-450 Ma), Salinic (445-422 Ma), Acadian (421-400 Ma) and Neoacadian (400-350 Ma) orogenies, respectively (van Staal et al., 2009, van Staal and Barr, 2012). Amalgamation of the Newfoundland Appalachians was completed by the arrival of the Avalonia microcontinent against the eastern trailing margin of Ganderia. The accretionary nature of the Appalachian orogen is such that orogenic events are polyphase (shown by e.g., overprinting relationships), and diachronous (e.g., closure at one margin may have been coeval with initial collision elsewhere). Thus, the precise time-space relationships of the distinct

orogenies are complex. For example, the western leading edge of Ganderia was still undergoing the late stages of the Salinic orogeny at the time of the onset of Acadian-related arc magmatism and deformation at its eastern trailing edge (van Staal et al., 2009; 2014).

The Ganderia microcontinent consists of Late Neoproterozoic-Ordovician arc and associated clastic metasedimentary rocks, whereas Avalonia comprises sub-greenschist facies Neoproterozoic volcanic, plutonic and sedimentary rocks overlain by Cambrian-Ordovician platform cover sequences (Hibbard et al., 2006; van Staal et al., 2009; van Staal and Barr, 2012). Though both microcontinents share Gondwanan affinity and Neoproterozoic basement, their distinct early Paleozoic geological records indicate that they were independent terranes prior to their amalgamation during the Acadian Orogeny (e.g. Murphy et al., 2002; van Staal et al., 1996).

The docking of lower plate Avalonia against upper plate Ganderia occurred along a NE-striking sinistral-oblique transpressional margin; in Newfoundland, the Ganderia-Avalonia suture coincides with the Dover Fault (Fig. 1; Blackwood and Kennedy, 1975; Dallmeyer et al., 1981; Holdsworth, 1994) and is correlated at depth with a geophysically-defined crustal-scale structure that offsets the Moho (Keen et al., 1986; Marillier et al., 1989; Stockmal et al., 1990). Sinistral shear is recorded in a ~20 km wide NE-striking zone of ductile shear that parallels the Dover Fault, the Wing Pond shear zone (Fig. 1; Holdsworth, 1994). Earliest sinistral shear was at least partly coeval with Silurian development of an eastward-increasing metamorphic field gradient within Ganderian rocks that reached sillimanite-grade at the terrane margin and was accompanied by anatexis and wide-spread syn-tectonic pluton emplacement (Holdsworth, 1994; D'Lemos et al., 1997). A subsequent narrow dextral ductile to brittle-ductile shear zone, the Dover Fault, formed under lower greenschist-facies conditions, locally overprinting the Silurian

Wing Pond shear zone (Holdsworth, 1994; D'Lemos et al., 1997). The post-tectonic Ackley Granite stitches the Dover Fault and provides a minimum age for displacement along the terrane boundary of 377 ± 4 Ma (Fig. 1; Kellett et al., 2014).

Whereas the general and relative timing of the Wing Pond and Dover Fault shear zones are established from magmatic rocks that exhibit syn-tectonic and cross-cutting relationships (Holdsworth, 1994), direct dating of different movement histories recorded by the mylonites has not previously been attempted. Although the docking of Avalonia against Ganderia is genetically associated to the Acadian Orogeny, the Silurian-Devonian deformation and metamorphism history of the eastern Ganderian margin and particularly the Wing Pond and Dover Fault shear zones may record components of Salinic, Acadian *and/or* Neoacadian events (e.g. Dunning et al., 1990; Holdsworth, 1994; Schofield and D'Lemos, 2000; van Staal, 1994; van Staal et al., 2009). Thus better timing constraints on sinistral and dextral shear episodes are imperative for elucidating the tectonic response of this plate boundary to the different accretionary events.

SAMPLE DESCRIPTIONS AND MICROSTRUCTURAL CHARACTERIZATION

Samples were collected from four granites that were syn-tectonically emplaced at the trailing edge of the Ganderia microcontinent, as well as fault gouge from the Hermitage Bay Fault, the interpreted southern extension of the Dover fault (Fig. 1). Each sample represents a different structural setting, in order to examine Ar systematics within different deformation regimes in the region of the Dover Fault (Fig. 2E). Sample locations are given in Table 1 and on Figure 1. White mica back-scattered electron (BSE) and chemical maps (Al, K, Ca, Fe and Si) were obtained and quantitative compositions calculated from electron microprobe analyses (summarized in Table 2, methods in supplementary data, full results in Table A1, Figs. A1-A4).

We also conducted a microstructural investigation of samples VL-12-NF-08, 12-KNA-002, 12-KNA-005 and 12-KNA-006, including quartz *c*-axis crystallographic fabric analysis, to constrain deformation conditions for the white mica. Thin sections of the samples collected were cut parallel the macroscopic stretching lineation and perpendicular to the dominant foliation (where present). Quartz *c*-axis orientations were determined using a Russell-Head Instruments G60 Automated Fabric Analyser. Quartz *c*-axis data from previous versions of the instrument, which have similar optical systems to the G60 used in this study, are indistinguishable from data generated using Electron Back-Scatter Diffraction Methods (Wilson et al., 2007; Peternell et al., 2010).

Granite dyke: Sample VL-12-NF-08

Sample VL-12-NF-08 was collected from a set of parallel granite dykes that cuts the main foliation in host Ganderian, Cambrian(?) to Ordovician metasandstone and sulfide-bearing metapelitic schist (Hibbard et al., 2006; Fig. 2A). In outcrop, the sampled dyke cuts S_0 and S_1 foliation in the host rocks and is aligned parallel to the axial plane (40˚→304˚ dip→dip direction) of ~1 m wavelength $F_{(2)}$ folds (Fig. 2A). The axial planar dykes are locally boudinaged whereas compositionally similar dykes oriented at high angle to S_2 are folded, albeit less tightly than the host rock. Combined, these relationships suggest that the dykes intruded during F_2 (Fig. 2E). The sample is a grey-coloured, pervasively foliated, fine-grained granite that contains quartz, plagioclase, K-feldspar, and white mica, as well as minor chlorite, garnet, staurolite, biotite and titanite and accessory apatite, monazite, xenotime and zircon (Fig. 3A, B). White mica, elongate skeletal staurolite, and chlorite form the foliation fabric (Fig. 3A), with white mica forming slender, 100-500 μm lathes with minor recrystallization at the tips evidenced by

mottled birefringence under crossed-polarized light (Fig. 3A inset). Though the white mica textures are indicative of recrystallization, chemical maps and compositional data indicate that the recrystallized mica is chemically identical to the igneous mica (see Fig. A3, Table A1 in the supplementary material), resulting in a single, homogeneous compositional population dominated by muscovite (87% on average) with minor components (generally <10%) of paragonite, Fe-celadonite and pyrophyllite (Table 2).

This sample has a well-developed foliation defined by aligned white mica and chlorite laths and discrete quartz lenses (Fig. 4A). There is also a strong compound C/S/C′fabric throughout demonstrating top-to-the-left (sinistral) shear (Fig. 4A). However, complex folding and refraction of foliations at the outcrop scale limit the usefulness of shear sense indicators at the thin section scale. Quartz within the sample is typically equigranular in size, with straight grain boundaries that intersect at 60˚/120˚ angles (Fig. 4A); characteristics consistent with static recrystallization and grain boundary area reduction (GBAR) processes. Though not common, there is local evidence of remnant bulging recrystallization. Quartz *c*-axes measured in the sample define an asymmetric, type-II crossed girdle fabric consistent with the top-to-the-left shear indicated by the C/S/C′fabric (Fig. 4A). The *c*-axis distribution indicates slip along the prism <a>, basal <a>, and rhomb <a> systems (Schmid and Casey, 1986).

K-feldspar granite: Sample 12-KNA-002

This sample is a protomylonite that originated as K-feldspar porphyritic white mica granite. The outcrop displays a steeply-dipping planar fabric with sinistral shear-sense indicators such as S-C’ fabric and sigma clasts (Fig. 2B). S planes are oriented 55˚→139˚, C’ planes are oriented 80˚→109˚, and the mineral lineation is 05˚→193˚ (plunge→trend), indicating a dominant NE-

SW oriented strike-slip system. The rock is pink and grey in colour, with large K-feldspar clasts carried in a grey mylonitic matrix, and contains quartz, K-feldspar, plagioclase, white mica, minor chlorite, epidote, titanite and trace zircon, pyrite and thorite (Fig. 3D). White mica wraps around feldspar grains and lines shear bands, and occurs as fine mats and locally as larger, 100-250 μm crystals, all indications of extensive dynamic recrystallization. However, as for VL-12-NF-08, chemical maps and compositional data indicate a relatively homogeneous compositional population (see Fig. A3, Table A1 in the supplementary material) dominated by muscovite, 72% on average, with a significant Fe-celadonite component of 25% on average, and the remainder paragonite and pyrophyllite (Table 2).

This sample exhibits a locally chaotic tectonic foliation defined by aligned mica laths and deformed quartz grains that commonly deflects around large feldspar porphyroclasts. Abundant shear sense indicators including the development of a compound C/S/C′fabric, extensional bands, and domino-type fragmented porphyroclasts all indicate top-to-the-left shear in thin section corresponding to NE-striking sinistral shear deformation in outcrop (Fig. 4B). Quartz within this specimen is typically elongate parallel to the foliation and is characterized by complex grain boundary relationships and internal subgrain development (Fig. 4B). These textures are consistent with dynamic recrystallization through bulging and subgrain rotation. Quartz *c*-axis orientation analyses yields a type-I crossed girdle fabric with a slight asymmetry that indicates top-to-the-left shear (sinistral movement across a NE-striking strike-slip fault) (Fig. 4B). The fabric itself is defined by movement dominantly along the prism <a> and rhomb <a> slip systems (Schmid and Casey, 1986).

Porphyritic granite dyke: Sample 12-KNA-005

This sample is pink and grey-coloured deformed K-feldspar porphyritic granite collected from a dyke that shallowly cuts fine-grained Cambrian(?) to Ordovician Ganderian mylonitic paragneiss and orthogneiss (Hibbard et al., 2006), indicating a pre- or syn-kinematic emplacement. The host mylonite exhibits a pervasive NE-striking, dextral S-C' fabric with supporting sigma clast shear-sense indicators (Fig. 2C). It has a dominant mylonite foliation of 82˚→117˚, and mineral lineation of 04˚→026˚, consistent with dextral strike-slip motion of the Dover Fault. Although we did not observe evidence for earlier sinistral strike-slip deformation at the sample site, the field location of this sample at the Ganderia-Avalonia boundary (Fig. 1) requires that it was pervasively deformed during the transpressional Ganderia-Avalonia collision and formation of the left lateral Wing Pond shear zone. The granite contains quartz, K-feldspar, plagioclase, white mica and biotite, with minor chlorite, ilmenite, and allanite, apatite and epidote-mantled monazite. Clasts of sericitized plagioclase and tartan-twinned K-feldspar, as well as 0.5-1 mm mica fish with undulose extinction, are wrapped by very fine grained quartz and recrystallized white mica (Fig. 3E, F). White mica and biotite are locally intergrown. Chemical maps and compositional data for this sample also reflect a homogeneous compositional population (Fig. A4, Table A1 of the supplementary material) comprising a muscovite component of 76% on average, a significant Fe-celadonite component of 20% on average, and minor paragonite and pyrophyllite components (Table 2).

The foliation in 12-KNA-005 is defined by aligned mica laths and quartz-dominated layers (Fig. 4C). An overall top-to-the-right shear in thin section, which corresponds to dextral shear sense along the NE-striking strike-slip fault in outcrop is defined by the asymmetry of sigma-type clasts (Fig. 4C). Quartz in this sample is inequigranular with interlobate grain boundaries; undulatory extinction is common. Evidence of bulging recrystallization occurs

commonly between grains while internal subgrains are developed within larger grains (Fig. 4C) indicating dynamic recrystallization. Though complex, grain boundaries commonly meet at triple-point junctions (Fig. 4C). This is consistent with at least minor GBAR static recovery recrystallization. Quartz *c*-axes define a diffuse, variably asymmetric, dominantly single-gridle fabric (Fig. 4C). The asymmetry of the fabric, which indicates dominant slip along the prism <a> and rhomb <a> systems (Schmid and Casey, 1986), is consistent with the observed shear sense indicators.

Late syn-tectonic granite: Sample 12-KNA-006

This sample was collected from a late syn-tectonic granite dyke 750 m NW from 12-KNA-005 that, like 12-KNA-005, also crosscuts Ganderian mylonitic paragneiss and orthogneiss within the Dover Fault, but at a higher angle (Fig. 2D). The dyke is locally pegmatitic, and its margins show metasomatic interaction with the host rock. The rock is pale pink, and relatively coarse-grained. It contains quartz, K-feldspar, plagioclase, white mica and chlorite, with minor biotite and titanite (Fig. 3G, H). A matrix of fine grained quartz wraps around sericitized plagioclase and tartan-twinned K-feldspar clasts. White mica and chlorite form anhedral laths and define a weak foliation. Chlorite contains abundant inclusions of titanite.

This sample lacks a well-defined foliation (Fig. 4D). Moreover, no clear, consistent shear sense indicators were observed in thin section. Quartz within 12-KNA-006 occurs as discontinuous pods between feldspar porphyroclasts (Fig. 4D). The grain themselves are inequigranular with interlobate grain boundaries. Bulging recrystallization is common between adjacent grains as is subgrain development both within grains and along grain margins (Fig. 4D). These textures are consistent with dynamic crystallization of quartz. Measured *c*-axis

orientations do not produce an interpretable pattern (Fig. 4D). This may reflect the discontinuous nature of the quartz within the specimen with each pocket being recrystallized within a local strain regime.

Harbour Breton Granite fault gouge: Sample KNA-013-017

This sample is clay-rich fault gouge sampled from brittle fault surfaces of the Hermitage Bay fault (Fig. 1). The host granitoid was mapped by O'Brien (1998) as the Harbour Breton Granite, dated at 575 ± 6 Ma (U-Pb zircon; Kellett et al., 2014). At the sampling site, the rock was pervasively dissected by moderate to steep brittle faults with chlorite and epidote common on slip surfaces. Slickenlines were common and variable, but preserved generally steep slip orientations.

METHODS AND RESULTS

U- Pb

Zircon and monazite were separated from several of the sampled granites using standard mineral separation techniques (Table 1; see supplementary data for full details). Grain mounts were prepared and polished to expose approximate mid-sections of the crystals. Individual grains were then imaged under BSE, as well as cathodoluminescence (CL) in those samples for which zircon exhibited a CL response, using a Zeiss EVO50 scanning electron microscope (SEM) operated at the Geological Survey of Canada (GSC) in Ottawa (representative grains shown in Fig. 5; all grains including U-Pb spot locations shown in Fig. A5). In general, zircon grains from VL-12-NF-08, 12-KNA-002 and 12-KNA-005 range in size from 100-500 μm, are subhedral, and contain few inclusions. Zircon from 12-KNA-002 and 12-KNA-005 exhibit concentric

oscillatory zoning visible both under BSE and CL-SEM imaging, while zircon from VL-12-NF-08 show cores with oscillatory, sector or convolute zoning, and dark-under-CL rims (Fig. 5). Monazite grains in 12-KNA-005 are anhedral, irregularly zoned, and range in size from 25-100 μm, and typically display resorbed edges mantled by elaborate post-kinematic coronas of apatite (inner rim), allanite (middle rim) ± epidote (outer rim) (Fig. 5f).

SHRIMP II (Sensitive High-Resolution Ion MicroProbe) U-Pb zircon and monazite analyses were conducted at the GSC in Ottawa over four analytical sessions. Full sample preparation, methodology and details of individual session are outlined in the supplementary data and Table A2. Spot selections, guided by BSE and CL-SEM images, were made to avoid fractures and inclusions, as well as to sample both core and rim regions of grains. Between 20 and 50 spots were analyzed for each sample. Long-term external reproducibility of secondary standards on the SHRIMP is 1% at the 2σ level for zircon, and thus dates are reported with a 2σ external error of 1%. Here and for all subsequent geochronological data, we use "date" to refer to results without implication of their geological significance, and "age" to refer to interpreted results.

VL-12-NF-08 zircon grains yielded two distinct, concordant U-Pb date populations (Fig. 5A,B). Eight analyses yielded high U contents > 2500 ppm (Table A2), and show a problematic correlation between date and U concentration characteristic for SHRIMP analyses (Fig. A6; Williams and Hergt, 2000). They are not considered further. Of the remaining data, twenty-seven analyses of zircon cores yielded a weighted mean $^{206}Pb/^{238}U$ date of 462.4 ± 5 Ma (MSWD = 1.6), while 15 rim analyses yielded a weighted mean date of 421.9 ± 4 Ma (MSWD = 1.9).

Zircon grains from 12-KNA-002 yielded generally concordant U-Pb data. Two analyses suggest possible inheritance of ca. 460 Ma zircon (Fig. 5C). The results provide a weighted mean ^{206}Pb-^{238}U date of 425.9 ± 4 Ma (MSWD = 0.52, n = 19) (Fig. 5C).

12-KNA-005 zircon grains also yielded a generally concordant dominant $^{206}Pb/^{238}U$ date population at 430.2 ± 4 Ma (MSWD = 0.86, n = 23) (Fig. 5E). This sample also displays a spread of a few analyses along concordia towards ca. 460 Ma, (n=4) as well as one concordant analysis at 1210 ± 10 Ma (Fig. 5D). These older analyses were all obtained from rare grains that exhibited distinct cores, and are interpreted to indicate two inherited zircon populations.

Monazite from sample 12-KNA-005 yielded concordant to slightly reversely discordant U-Pb data (Fig. 5F). The individual ^{206}Pb-^{238}U spot dates range from 403 ± 5 Ma to 429 ± 5 Ma. The weighted mean date of the dated population is 417 ± 5 Ma (n=26), but high MSWD of 3 indicates that they do not characterize a single age population (Fig. 5G).

Step heat $^{40}Ar/^{39}Ar$

White mica was separated from samples by standard crushing, washing and sieving procedures (see full details in the supplementary data). Mineral grains selected for dating ranged in size from 250-500 µm. Individual grains were visually inspected under a microscope and selected based on purity (e.g., apparent lack of inclusions, mineral intergrowths or alteration).

Hand-picked mineral separates were irradiated at the McMaster nuclear reactor facility (GSC irradiation #66) for 160 MWh, operating at 2.5 MW. Following irradiation, individual grains were selected, loaded into a copper planchet and placed into an all-metal, ultra-high vacuum line. Samples were step-heated using a Photon Machines CO_2 laser and analyzed using a Nu Instruments Noblesse mass spectrometer housed at the Geological Survey of Canada, Ottawa.

White mica grains were heated over 20-25 heating steps. Between one and three single-grain aliquots of each mineral separate were step-heated, with replicates providing a gauge of within-sample variability. Irradiation flux was monitored using Fish Canyon tuff sanidine (FCT-SAN) (28.305 ± 0.036 1σ Ma; Renne et al., 2010). Analytical details are described in the supplementary data and follow Kellett and Joyce (2014). Data collection and data reduction were carried out using MassSpec software version 7.93 (Deino 2001). All $^{40}Ar/^{39}Ar$ results (step heating and *in situ*) were calculated using the decay constant of Min et al. (2000). Results of the step heating experiments are recorded in Table A3 and Figure 6. Plateau dates were calculated using MassSpec software, and defined using the following criteria: at least three contiguous heating steps that are within 2σ error and that comprise ≥50% of ^{39}Ar released.

A muscovite crystal from sample VL-12-NF-08 yielded a plateau date of 399 ± 3 Ma (n = 12, 83.5% of ^{39}Ar released, MSWD = 0.7) (Fig. 6A). Older initial and final steps indicate minor heterogeneity. Ca/K and Cl/K ratios determined from measurement of $^{37}Ar_{Ca}$ and $^{38}Ar_{Cl}$ were monitored to indicate the presence of impurities or contribution of fluid inclusions; in this case, Ca/K and Cl/K are negligible indicating insignificant contamination.

Two muscovite grains from 12-KNA-002 yielded extremely heterogeneous Ar release spectra (Fig. 6B). Small spikes in the Ca/K ratio indicate some contamination. Aliquot 2 yielded three times the volume of gas of Aliquot 1, producing a more precise measurement. This grain yielded step heat dates predominantly ranging from ca. 385-420 Ma, with few younger initial heating steps and one older, small volume gas step in the final 10% of ^{39}Ar released. In general, 89% of ^{39}Ar released from both aliquots yielded dates between 384-432 Ma. Integrated dates for aliquots 1 and 2 are 402 ± 3 Ma and 399 ± 2 Ma, respectively.

Three grains of muscovite from 12-KNA-005 were step-heated, two of which yielded plateau dates (Fig. 6C). Aliquot 1 yielded a plateau date of 383 ± 2 Ma (n = 4, 51.4% of ^{39}Ar released, MSWD = 1.8), while Aliquot 3 yielded 388 ± 2 Ma (n = 13, 94.2% of ^{39}Ar released, MSWD = 1.6). In general, the spectra from the three grains show negligible Ca/K and Cl/K ratios, and slightly heterogenous, but similar spectra. Integrated dates for the grains are 387 ± 2 Ma, 396 ± 2 Ma and 389 ± 2 Ma for Aliquots 1, 2 and 3, respectively.

Two muscovite grains from 12-KNA-006 yielded generally uniform Ar release spectra, with plateau dates of 390 ± 2 Ma (Aliquot 1, n = 11, 89.5% of ^{39}Ar released, MSWD = 1.2) and 385 ± 2 Ma (Aliquot 2, n = 7, 82.4% of ^{39}Ar released, MSWD = 1.1) (Fig. 6D). Ca/K and Cl/K ratios for both aliquots are negligible. Integrated dates for Aliquots 1, and 2 are 391 ± 3 Ma and 384 ± 2 Ma, respectively.

In general, inverse isochron plots for all four samples show data clustered near the radiogenic axis, with little spread, and no clear indication of excess or non-atmospheric extraneous Ar (Fig. A7).

In-situ ^{40}Ar/^{39}Ar

In-situ laser ablation analyses were performed at The Open University, UK. Polished slabs of 150 µm thickness and maximum size 5x5 mm were washed in acetone and distilled water before packing into aluminium foil packets for irradiation. All samples were irradiated at McMaster University in Canada with irradiation batch McM87 for 400 MWH operating at 2.9 MW. *In-situ* laser ablation was achieved using a New Wave 213 nm Nd-YAG ultra-violet laser coupled to an automated gas handling vacuum system and admitted into a Nu Instruments Noblesse noble gas mass spectrometer. Data were reduced using an in-house software package (ArMaDiLo), and

plotted using Isoplot (Ludwig, 2003). GA1550 biotite standard with an age of 99.77 ± 0.11 1σ Ma (normalized to Fish Canyon tuff sanidine (FCT-SAN) at 28.305 ± 0.036 1σ Ma) was used as a flux monitor (Renne et al., 2010). Data are presented at the 95% confidence level, all results are quoted at 2σ and uncertainties on measurements are 1σ. Complete analytical details including representative blanks are described in the supplementary data (Table A4).

Twenty-four $^{40}Ar/^{39}Ar$ spot dates were obtained from five muscovite grains in disc CA 7-1, sample VL-12-NF-08 (Table 3; Fig. 7A,B). The spot analyses yield a spread of dates ca. 410-383 Ma with a weighted mean date of 396.6 ± 2.5 Ma (n = 24, MSWD = 10). There is no apparent intragrain correlation between $^{40}Ar/^{39}Ar$ date and location of analysis for traverses across grains G and H: adjacent within-grain analyses in all three grains shown in Fig. 7D differ by up to 13 myr (e.g. spots H.6 and H.7, G.3 and G.4). Grain F shows a weak relationship of older core and younger rim, indicated with a best fit line in Fig. 7D, although grains H and G do not. Although all grains yielded ca. 395 Ma dates, the two smallest grains yielded only younger dates (≤395 Ma), while older dates were obtained from large grains F, G and H. Thus there is an apparent relationship between grain size and date distribution, but evidence for intragrain diffusion profiles is inadequate.

Twenty-seven spot $^{40}Ar/^{39}Ar$ dates were collected from *in situ* muscovite grains situated within disc CA 1-3 from sample 12-KNA-002 (Fig. 8A,B). However, 7 of those yielded ^{40}Ar counts <2x background levels and are considered unreliable. The spot dates of the remaining 20 analyses range from ca. 399 to ca. 370 Ma, with a weighted mean date of 385 ± 4 Ma (MSWD = 18). As for sample VL-12-NF-08, adjacent analyses differ by >10 myr (e.g. spots 2.3 and 2.4), however in this case the analyses are likely from different but adjacent grains within mica-rich shear bands. There is no apparent relationship between date and structural position, with all shear

bands yielding a large range in $^{40}Ar/^{39}Ar$ date. ^{37}Ar measurements were high for many spots in this sample, suggesting pervasive contamination or impurities.

Twenty-nine spot $^{40}Ar/^{39}Ar$ dates were analyzed from muscovite grains within disc CA 4-5, sample 12-KNA-005 (Fig. 9A,B). The population of spot dates ranges from 404 to 383 Ma, excluding two far outliers, 423 and 359 Ma, which were not reproducible and are not considered further. The weighted mean date for this sample is 392 ± 2 Ma (MSWD = 13). As for 12-KNA-002, adjacent analyses differ, in this case by >20 myr (e.g., spots 5.1, 5.2).

K-Ar

Dating of fine grained minerals (< 2 μm) such as illite can provide constraints on timing of active retrograde fault movement in the shallow crust (van der Pluijm et al., 2001; Zwingmann and Mancktelow, 2004; Zwingmann et al., 2010, Pleuger et al., 2012). K-Ar dating is a reliable tool to constrain authigenic formation of fined-grain illite clay minerals in brittle faults to circumvent ^{39}Ar recoil by $^{40}Ar/^{39}Ar$ dating (Clauer et al., 2012, Torgersen et al., 2015).

Clay separation and characterization of sample KNA-013-017 was performed at the GSC (see supplementary data for details). Semi-quantitative X-ray diffraction analysis (mineral ratio percent) yielded the following approximate composition: 70% chlorite, 20% muscovite, 4% K-feldspar, 3% plagioclase and 3% calcite (Fig. A7). K-Ar analysis of the clay fraction at CSIRO (Commonwealth Scientific and Industrial Research Organization, Australia) yielded a date of 350.6 ± 7.0 Ma (Table 4).

Deformation Temperatures

The opening angle of crossed-girdle quartz *c*-axis fabric may be related to the temperature at which the fabric was established (Kruhl, 1998; Morgan and Law, 2004; Law, 2014). Employing the opening-angle thermometer, however, requires a number of assumptions including temperature being the primary control, stable critical resolved shear stress, lack of hydrolytic weakening, and consistent strain rate (see Law (2014) for a detailed review).

Of the samples analysed for *c*-axis fabric in this study only two yielded crossed girdle fabrics. The opening angle for the *c*-axis fabric of VL-12-NF-08 is estimated at ~ 50˚ (Fig. 4A), which corresponds to a deformation temperature of 385 ± 50˚C, while the opening angle for 12-KNA-002 is estimated at ~46˚ (Fig. 4B), corresponding to a deformation temperature of 350 ± 50˚C. These temperatures are consistent with the general range at which bulging recrystallization and minor subgrain rotation recrystallization occur in other, well-studied shear zones (see Stipp et al. 2002).

DISCUSSION

Interpretation of age data

Zircon U-Pb results in samples VL-12-NF-08, 12-KNA-002 and 12-KNA-005 are consistent with magmatic crystallization during the Silurian. These bodies are part of a larger suite of S-type syn-tectonic granites, derived from partial melting of Ganderian metasedimentary rocks (e.g., Kerr, 1997). They therefore record the presence of partial melt during ca. 430-422 Ma and in the case of VL-12-NF-08, D_2 syn-kinematic crystallization at 422 ± 4 Ma, both consistent with previously published ages for peak metamorphism and synkinematic granite emplacement (Dunning et al., 1990). Clearly defined inheritance in VL-12-NF-08 zircon, and suggestions of similar inheritance in 12-KNA-002 and -005 zircon, indicate the source rock(s)

contained a ca. 462 Ma age population. This age is well represented locally (e.g., Dunning et al., 1990; Valverde-Vaquero et al., 2006), and coincides in time with development of the Exploits back-arc basin, suggesting either a structural juxtaposition of Ganderia over the back arc, or expansion of back-arc magmatism into the adjacent Ganderian passive margin.

Monazite U-Pb data in 12-KNA-005 indicate subsequent and prolonged (re-)crystallization of monazite between 429-403 Ma. Field relationships of the Silurian granite suite indicate that it was pervasively deformed by the broad, NE-striking, sinistral Wing Pond shear zone under relatively high-temperature metamorphic conditions (Schofield and D'Lemos, 1998). We therefore suggest that monazite recrystallization was facilitated by sinistral ductile shear conditions in which mylonite developed across a wide swath of Ganderia's trailing edge.

$^{40}Ar/^{39}Ar$ dates of mica from all three samples (both step heat and *in situ*) are ≥30 myr younger than the igneous (U-Pb zircon) age of the granites, with the oldest *in situ* dates in VL-12-NF-08 and 12-KNA-005 overlapping with the youngest monazite U-Pb dates at ca. 400 Ma. This reset of Ar occurred at a regional rather than local scale, and we interpret it to reflect efficient removal of Ar via recrystallization, deformation, fluid interaction and thermal diffusion of Ar in white mica prior to ca. 400 Ma during cooling from magmatic and peak metamorphic conditions.

The foliation fabric in VL-12-NF-08 is defined by dynamically-recrystallized quartz and mica fish, with deformation occurring at ca. 385 ± 50 °C, indicating latest deformation of the dyke occurred post-peak metamorphic conditions (interpreted at ca. 422 Ma, Dunning et al. (1990) and this work), during cooling of the metamorphic host rocks. The close correspondence between the step heat plateau date of 399 ± 3 Ma and mean *in situ* spot date of 397 ± 2.5 Ma, the weakly-defined apparent diffusion profile preserved in the largest (by volume) grain analyzed,

and the apparent grain size-age relationship could be argued as evidence that white mica in this sample preserves cooling ages.

Using the program DiffArgP (Warren et al., 2012b, Wheeler, 1996), and diffusion parameters recommended in Harrison et al. (2009) we forward-modelled ideal Ar diffusion profiles in white mica for various cooling scenarios (see details in the Supplementary data). We determined that a linear cooling rate of -5 °C/Ma will produce a core to rim age difference of >10 myr in a 500 µm diameter grain, similar to that observed in grain F (note that a linear cooling rate of -10 °C/Ma for an equivalent grain would produce an age gradient of ~5 myr). These conditions (linear cooling rate of -5 °C/Ma from 520 °C) yield a bulk grain Ar closure temperature of ~440 °C. Therefore the $^{40}Ar/^{39}Ar$ data for this sample could predominantly reflect diffusive Ar closure between ca. 405-395 Ma, following regional peak metamorphism, with younger *in situ* dates reflecting a grain size control on closure temperature. For example, the same diffusion experiment conducted for a 250 µm diameter grain suggest a ca. 4 myr younger bulk age for a -5 °C/Ma cooling rate than for a 500 µm grain, which is sufficient to explain the apparent grain size-date relationship in VL-12-NF-08 (Fig. 7).

However, an alternative interpretation of ^{40}Ar loss via grain rim recrystallization and intragrain deformation in the absence of thermal diffusion is also possible (Mulch et al., 2005; Cosca et al., 2011). For example, Mulch et al. (2005) studied mylonite-hosted mica fish and found a core to rim date relationship that they attributed to recrystallization during deformation. Step heat experiments of the mica fish yielded plateau dates that masked the intragrain date variations. In their study, chemical zoning with a stepped date profile across zones aided in distinguishing recrystallization-induced loss of Ar versus thermal diffusion loss of Ar. We did not observe chemical zoning in white mica to aid in our interpretation. However, the patchy age

zonation, spanning 25 myr, and general lack of bell-shaped Ar loss profiles suggest that thermal diffusion of Ar was not a controlling process, at least post ca. 410 Ma, the oldest spot age from this sample (e.g. Villa, 2015; 2016). Since latest deformation in this sample occurred below the ideal Ar closure temperature (385 °C vs. ≥420 °C, dependent upon grain size and cooling rate), the distribution of $^{40}Ar/^{39}Ar$ dates preserved in this sample more likely record deformation-induced Ar loss via syn-kinematic dynamic recrystallization and/or internal deformation of white mica grains, resulting in the observed complex/patchy Ar distribution pattern (Cosca et al., 2011).

The mylonite deformation fabric in 12-KNA-002 indicates NE-striking sinistral shear, with syn-kinematic white mica undergoing associated deformation at 350 ± 50 °C. Assuming a similar cooling rate and grain size range to VL-12-NF-08, sinistral shear occurred well below the closure temperature for Ar diffusion in 12-KNA-002. Thus *in situ* $^{40}Ar/^{39}Ar$ dates should record post-cooling syn-kinematic recrystallization (e.g., di Vincenzo et al., 2007). I*n situ* results show the same pattern of Ar reset at ca. 400 Ma as for VL-12-NF-08. However, the step heating spectra are quite heterogenous in this sample (Fig. 7B), the *in situ* analyses indicate high $^{37}Ar_{Ca}$, and the younger analyses are of lower quality (lower ^{40}Ar, and higher ^{36}Ar counts). Further, the youngest *in situ* $^{40}Ar/^{39}Ar$ dates are equivalent in age to, and in cases younger than, the Ackley Granite that stitches the Dover Fault (Fig. 10). These characteristics all point to the likely influence of fluids and fluid alteration on the white mica Ar concentrations. Epidote, commonly occurring in this sample in patches within shear bands, and replacing plagioclase (Fig. 3D), is found locally throughout this region of Newfoundland. Such epidote is considered an alteration mineral indicative of hypabyssal hydrothermal circulation cells and related W, Mo, F and base metal mineralization that developed during and following emplacement of the Devonian post-

tectonic plutonic suite (e.g., Kerr et al., 2009; Kellett et al., 2014). Fluid infiltration during emplacement of the Devonian post-tectonic granite suite therefore likely modified ^{40}Ar reservoirs in the syn-kinematic white mica of this sample. In other words, the white mica behaved as a hygrochronometer (Villa, 2016). Although the most recent geological map of the region (Fig. 1) does not show a Devonian pluton in close proximity to 12-KNA-002, the nearby Devonian Maccles Lake granite has unknown extent towards the northwest (Kellett et al., 2014) and may have produced a local circulation cell. Further, minor epidote was also observed in 12-KNA-005, forming the outermost rims of post-kinematic allanite-apatite±epidote coronas around monazite. Thus the mylonite zones appear to have acted as fluid pathways. We tentatively propose, therefore, that latest sinistral shear occurred at ca. 394 Ma (n= 6), corresponding to the oldest, most pristine *in situ* data, and consistent with sinistral shear predating both dextral shear and the Ackley pluton. However, further testing is required from an area not affected by post-deformation hydrothermal circulation. The spread towards younger dates records fluid-assisted partial to complete Ar loss at ca. 380-375 Ma.

Both 12-KNA-005 and 12-KNA-006 show field relationships indicating development of the dextral Dover Fault (Fig. 2E). Sample 12-KNA-005 was collected from a shallowly cross-cutting granite dyke indicating it was emplaced pre- to syn-deformation, with supporting U-Pb zircon results indicating emplacement at 430 Ma. Sample 12-KNA-006 was sampled from a latest syn-deformation cross-cutting dyke (Fig. 2C, D). These relationships are reinforced by the microstructures: 12-KNA-005 exhibits a record of well-developed non-coaxial strain while 12-KNA-006 is weakly deformed and lacks a well-defined foliation (Fig. 4D). Step heating results from three single crystals in 12-KNA-005 yield somewhat heterogeneous Ar release spectra, and discordant results. However all results are within the range of *in-situ* dates, which span 404-383

Ma. Although the range of *in situ* $^{40}Ar/^{39}Ar$ dates from 12-KNA-005 is similar to VL-12-NF-08, the distribution within that range is dissimilar. The mean *in situ* date is significantly younger in 12-KNA-005, as are the step heat plateau dates. The youngest steps yield a weighted average date of 385.9 ± 1.7 Ma (n = 9) interpreted as recording latest dextral slip on the Dover Fault. This is compatible with late emplacement and cooling of 12-KNA-006 by 385 ± 2 Ma.

Fault gouge clay from the Hermitage Bay Fault comprises two K-bearing phases, detrital K-feldspar and illite. The weakly crystalline nature of the illite (Fig. A8, supplementary data) suggests it is primarily authigenic, although a detrital component cannot be ruled out. The resulting K-Ar date for clay fraction of the fault gouge, 351 ± 7 Ma, is therefore interpreted as a maximum age for latest motion along the fault. This result indicates that brittle deformation at the Ganderian margin extended at least into the Carboniferous.

Implications for Ar behavior in deformed rocks and shear zones

It is apparent from this dataset that the step-wise release of Ar from white mica can homogenize or obscure important age information in deformed rocks, as has previously been suggested (c.f., Mulch et al., 2005). In this case, the step-heat data neither yielded evidence for the oldest *in-situ* dates (e.g. 12-KNA-002, 12-KNA-005) corresponding to the timing of recrystallization or cooling of the samples, nor the youngest *in-situ* dates (e.g. VL-12-NF-08, 12-KNA-002) which provide age constraints on deformation and fluid events. The igneous and recrystallized white mica populations in all three samples analyzed for chemistry were chemically indistinguishable. This lack of chemical zoning between igneous and recrystallized white mica may have played a role in the homogenization of age populations during step heating, since mica chemistry appears to be a major control on the temperature-controlled release of Ar in

step heating experiments (Allaz et al., 2011). In contrast, the *in situ* $^{40}Ar/^{39}Ar$ information was valuable in interpreting the timing of cooling/recrystallization, deformation and fluid events. However, *in situ* $^{40}Ar/^{39}Ar$ analysis is not always an available tool; depending on the age of the region under investigation, and the size of the target grains, *in-situ* analyses may pose an analytical challenge due to low signal-to-blank ratios (e.g. Cossette et al., 2015). In those cases, acquiring single grain fusion $^{40}Ar/^{39}Ar$ data may be a preferable compromise to multigrain or even single grain step heating analyses. This procedure should minimize or at least characterize potential 'age homogenization', though it may still impact interpretation of the resulting $^{40}Ar/^{39}Ar$ dates (e.g., Mottram et al., 2015). At a minimum, the interpretation of $^{40}Ar/^{39}Ar$ step heat data from deformed rocks should be guided by a temporal framework derived from other chronometers, and including constraints on the conditions and relative timing of deformation and metamorphism. If deformation occurred at temperatures at which thermal diffusion of Ar was efficient, then a plateau date calculated from Ar release spectra may well relate to the timing of cooling. However, if deformation occurred under conditions at which thermal diffusion of Ar was inefficient, a plateau date may just represent the mean of a mixed age population and lack geological significance. *In situ* $^{40}Ar/^{39}Ar$ data can provide meaningful constraints on the timing and duration of deformation events, but are best interpreted in the context of field, microstructural, petrographic and multi-isotopic data.

Constraints on timing of NE-striking sinistral and dextral shear at the Ganderia/Avalonia suture

The results from this study, summarized in Fig. 10, can be used to reconstruct the deformation history of the trailing edge of the Ganderian microcontinent during the Salinic,

Acadian and Neoacadian orogenies and provide the first direct timing constraints on the Ganderia-Avalonia suture structures in Newfoundland. Zircon inheritance from a ca. 462 Ma source rock corresponds with the timing of back-arc magmatism on the Ganderian margin (e.g. Valverde-Vaquero et al., 2006). This suggests that Gander Group rocks of eastern Ganderia overlie intra-Ganderian Tetagouche-Exploits backarc basin rocks. One zircon grain indicating 1.2 Ga inheritance provides further support for the presence of Mesoproterozoic basement beneath Ganderia (van Staal et al., 2012). Syn-tectonic (D_2) partial melting of the trailing Ganderian margin spanned at least 430-422 Ma, coinciding with Salinic closure of the intra-Ganderian Tetagouche-Exploits backarc basin, reassembly of Ganderia, and peak metamorphism at Ganderia's trailing edge. Sinistral (±dextral) shear facilitated the Acadian transpressional accretion of Avalonia to Ganderia, forming the post-peak metamorphic, NE-striking Wing Pond shear zone between ca. 422-394 Ma. Based on structural relationships, Holdsworth (1994) interpreted a switch from sinistral to dextral shear to have occurred during Silurian. We cannot rule out a Silurian shear reversal event based on our data. However, we propose that latest sinistral motion of the Wing Pond shear zone occurred at ca. 394 Ma. This is compatible with the conclusions of Willner et al. (2015), who have argued that the Neoacadian (400-365 Ma) arrival of Meguma terrane to composite Laurentia along a dextral transpressional boundary produced a conjugate sinistral shear zone that facilitated escape of the Mira terrane of Cape Breton Island, and Newfoundland Avalonia to the NW (present day coordinates). This conjugate system was short lived, as a Devonian shear reversal is recorded in Newfoundland, forming the narrower and lower temperature, NE-striking dextral Dover Fault by 385 Ma. The late to post-tectonic Devonian granite suite was emplaced during Middle to Late Devonian, stitching the Dover Fault at ca. 377 ± 4 Ma and forming local hydrothermal circulation cells and related mineralization.

Brittle slip along the broadly collinear Hermitage Bay Fault persisted into the Mississippian, likely part of a regional network of reactivated Appalachian-trend (NE-SW oriented) structures interpreted to have produced the transtensional Maritimes Basin (Waldron et al., 2015).

CONCLUSIONS

$^{40}Ar/^{39}Ar$ dating of white mica, and complementary U-Pb dating of zircon and monazite and K-Ar dating of fault gouge from granite bodies deformed at the Ganderia-Avalonia boundary in Newfoundland was conducted to study the influence of deformation and fluids on Ar behavior in white mica. Syn-kinematic, collision-related granites were emplaced during peak metamorphic conditions of the Salinic orogeny at 430-422 Ma, recorded by igneous zircon. Recrystallised monazite and white mica record relatively high temperature left-lateral high strain deformation until perhaps as late as ca. 394 Ma, forming the NE-striking Wing Pond shear zone. Ar loss in white mica during shear likely occurred via both thermal diffusion and recrystallization. Low temperature dextral reactivation of a narrow segment of the high strain zone, the Dover Fault, occurred at ca. 385 Ma. The Ganderia-Avalonia boundary was stitched by the post-tectonic Ackley Granite at 377 ± 4 Ma (Kellett et al., 2014), one of a large suite of post-tectonic plutons. Related hypabyssal hydrothermal circulation cells locally altered white mica and induced loss of radiogenic Ar. Authigenic illite in fault gouge of the Hermitage Bay Fault indicates that slip along Appalachian-trend structures persisted until at least the Mississippian.

The step-wise release of Ar from white mica homogenized and obscured spatially-controlled Ar isotope reservoirs in the sheared rocks, in cases yielding plateau dates of equivocal geological significance. In situ $^{40}Ar/^{39}Ar$ analysis is the preferred method for dating the timing of deformation recorded by white mica.

ACKNOWLEDGEMENTS

We gratefully acknowledge laboratory assistance from Nancy Joyce, Nicole Rayner, Tom Pestaj, Jeanne Percival, Igor Bilot, Alain Grenier, Pat Hunt, Sam Hammond, Alison Halton and James Malley, as well as fruitful discussions in and out of the field with Andrew Kerr and Giorgio Ruberti. This research was funded by the Targeted Geoscience Initiative program of Natural Resources Canada, and is GSC contribution #20150445. Reviews by Alex Zagorevski and two anonymous reviewers are most appreciated.

REFERENCES

Allaz, J., Engi, M., Berger, A., Villa, I.M., 2011. The effects of retrograde reactions and of diffusion on ^{40}Ar-^{39}Ar ages of micas. Journal of Petrology, 52, 691-716.

Blackwood , R.F., Kennedy, M.J., 1975. The Dover Fault: western boundary of the Avalon zone in northeastern Newfoundland. Canadian Journal of Earth Sciences, 12, 320-325.

Bröcker, M., Baldwin, S., Arkudas, R. (2013). The geological significance of ^{40}Ar/^{39}Ar and Rb–Sr white mica ages from Syros and Sifnos, Greece: a record of continuous (re) crystallization during exhumation? Journal of Metamorphic Geology, 31(6), 629-646.

Clauer, N., Zwingmann, H., Liewig, N., Wendling, R. 2012. Comparative 40Ar/39Ar and K-Ar dating of illite-type clay minerals. Earth Science Reviews, 115, 76–96, doi: 10.1016/j.earscirev.2012.07.003.

Cosca, M., Stunitz, H., Bourgeix, A.L., Lee, J.P., 2011. ^{40}Ar* loss in experimentally deformed muscovite and biotite with implications for ^{40}Ar/^{39}Ar geochronology of naturally deformed rocks. Geochimica et Cosmochimica Acta, 75, 7759-7778.

Cossette, É., Schneider, D.A., Warren, C.J., Grasemann, B., 2015. Lithological, rheological, and fluid infiltration control on ^{40}Ar/^{39}Ar ages in polydeformed rocks from the West Cycladic detachment system, Greece. Lithosphere, 7, 189-205.

D'Lemos, R.S., Schofield, D.I., Holdsworth, R.E. King, T.R., 1997. Deep crustal and local rheological controls on the siting and reactivation of fault and shear zones, northeastern Newfoundland. Journal of the Geological Society, 154, 117-121.

di Vincenzo, G., Carosi, R., Palmeri, R., Tiepolo, M., 2007. A comparative U-Th-Pb (zircon-monazite) and ^{40}Ar-^{39}Ar (muscovite-biotite) study of shear zones in northern Victoria Land (Antarctica): implications for geochronology and localized reworking of the Ross Orogen. Journal of Metamorphic Geology, 25, 605-630.

Dallmeyer, R.D., Blackwood, R.F., Odom, L., 1981. Age and origin of the Dover Fault: tectonic boundary between the Gander and Avalon Zones of the northeastern Newfoundland Appalachians. Canadian Journal of Earth Sciences, 18, 1431-1442.

Deino, A.L., 2001. Users manual for Mass Spec v. 5.02. Berkeley Geochronology Center Special Publication 1a, 119 p.

Dunning, G.R., O'Brien, S.J., Colman-Sadd, S.P., Blackwood, R.F., Dickson, W.L., O'Neill, P.P., Krogh, T.E., 1990. Silurian orogeny in the Newfoundland Appalachians. Journal of Geology, 98, 895-913.

Forster, M.A., Lister, G.S., 2014. $^{40}Ar/^{39}Ar$ geochronology and the diffusion of ^{39}Ar in phengite-muscovite intergrowths during step-heating experiments in vacuo. Geological Society, London, Special Publications, 378, 117-135.

Harrison, T.M., Celerier, J., Aikman, A.B., Hermann, J., Heizler, M.T., 2009. Diffusion of ^{40}Ar in muscovite. Geochimica et Cosmochimica Acta, 73, 1039-1051.

Hibbard, J.P., van Staal, C.R., Rankin, D.W., Williams, H., 2006. Geological Survey of Canada, "A" Series Map 2096A, 2 sheets, doi:10.4095/221912.

Holdsworth, 1994. Structural evolution of the Gander-Avalon terrane boundary: a reactivated transpression zone in the NE Newfoundland Appalachians. Journal of the Geological Society, London, 151, 629-646.

Keen, C.E., Keen, M.J., Nichols, B., Reid, I., Stockmal, G.S., Colman-Sadd, S.P., O'Brien, S.J., Miller, H., Quinlan, G., Williams, H., Wright, J., 1986. Deep seismic reflection profile across the northern Appalachians. Geology, 14, 141-145.

Kelley, S., 2002. Excess argon in K-Ar and Ar-Ar geochronology. Chemical Geology, 188, 1-22.

Kellett, D.A., Joyce, N., 2014. Single- and multi-collection $^{40}Ar/^{39}Ar$ measurements for conventional step-heating and total fusion age calculation using the Nu Noblesse at the Geological Survey of Canada: analytical details. Geological Survey of Canada, Technical Note 8, 27 p, doi:10.4095/293465.

Kellett, D.A., Rogers, N., McNicoll, V., Kerr, A., van Staal, C., 2014. New age data refine extent and duration of Paleozoic and Neoproterozoic plutonism at Ganderia-Avalonia boundary, Newfoundland. Canadian Journal of Earth Sciences, 51, 943-972.

Kerr, A., 1997. Space-time composition relationships among Appalachian-cycle plutonic suites in Newfoundland, in Sinha, A.K., Whalen, J.B., and Hogan, J.P., eds., The Nature of Magmatism in the Appalachian Orogen. Boulder, Colorado, Geological Society of America Memoir 191, 193-219.

Kerr, A., van Nostrand, T., Dickson, W.L., Lynch, E.P., 2009. Molybdenum and tungsten in Newfoundland: a geological overview and a summary of recent exploration developments. *In* Current Research, Newfoundland and Labrador Department of Natural Resources, Geological Survey, Report 09-1. pp. 43–80.

Kramar, N., Cosca, M.A., and Hunziker, J.C., 2001. Heterogeneous $^{40}Ar^*$ distributions in naturally deformed muscovite: in situ UV-laser ablation evidence for microstructurally controlled intragrain diffusion. Earth and Planetary Science Letters, 192, 377-388.

Kruhl, J.H., 1998. Prism- and basal-plane parallel subgrain boundaries in quartz: a microstructural geothermobarometer: Reply. Journal of Metamorphic Geology, 16, 142–146.

Kula, J., Spell, T.L., 2012. Recovery of muscovite age gradients by $^{40}Ar/^{39}Ar$ vacuum furnace step-heating analysis. Chemical Geology, 304, 166-174.

Law, R.D., 2014. Deformation thermometry based on quartz c-axis fabrics and recrystallization microstructures: A review. Journal of Structural Geology, 66, 129–161. doi:10.1016/j.jsg.2014.05.023

Ludwig, K.R., 2003. User's manual for Isoplot/Ex rev. 3.00: a Geochronological Toolkit for Microsoft Excel. Special Publication, 4, Berkeley Geochronology Center, Berkeley, 70 p.

Marillier, F., Keen, C.E., Stockmal, G.S., Quinlan, G., Williams, H., Colman-Sadd, S.P. O'Brien, S.J., 1989. Crustal structure and surface zonation of the Canadian Appalachians: implications of deep seismic reflection data. Canadian Journal of Earth Sciences, 26, 305-321.

McWilliams, C. K., Kunk, M. J., Wintsch, R. P., Bish, D. L., 2013. Determining ages of multiple muscovite-bearing foliations in phyllonites using the $^{40}Ar/^{39}Ar$ step heating method: Applications to the Alleghanian orogeny in central New England. American Journal of Science, 313(10), 996-1016.

Mottram, C.M., Warren, C.J., Halton, A.M., Kelley, S.P., Harris, N.B.W., 2015. Argon behavior in an inverted Barrovian sequence, Sikkim Himalaya: the consequences of temperature and timescale on $^{40}Ar/^{39}Ar$ mica geochronology. doi:10.1016/j.lithos.2015.08.018

Min, K., Mundil, R., Renne, P.R., Ludwig, K.R., 2000. A test for systematic errors in $^{40}Ar/^{39}Ar$ geochronology through comparison with U-Pb analysis of a 1.1 Ga rhyolite. Geochimica et Cosmochimica Acta, 64, 73-98.

Monié, P., 1990. Preservation of Hercynian $^{40}Ar/^{39}Ar$ ages through high-pressure low-temperature Alpine metamorphism in the Western Alps. European Journal of Mineralogy, 2, 343-361.

Morgan, S.S., Law, R.D., 2004. Unusual transition in quartzite dislocation creep regimes and crystal slip systems in the aureole of the Eureka Valley-Joshua Flat-Beer Creek pluton, California: a case for anhydrous conditions created by decarbonation reactions. Tectonophysics, 384, 209–231. doi:10.1016/j.tecto.2004.03.016

Mulch, A., Cosca, M.A., 2004. Recrystallization or cooling ages: in situ UV-laser $^{40}Ar/^{39}Ar$ geochronology of muscovite in mylonitic rocks. Journal of the Geological Society, 161, 573-582.

Mulch, A., Cosca, M.A., Andresen, A., Fiebig, J., 2005. Time scales of deformation and exhumation in extensional detachment systems determined by high-spatial resolution in situ UV-laser $^{40}Ar/^{39}Ar$ dating. Earth and Planetary Science Letters, 233, 375-390.

Murphy, J.B., Nancy, R.D., Keppie, J.D., 2002. Discussion and reply: West African proximity of the Avalon terrane in the latest Precambrian. Geological Society America Bulletin, 114, 1049–11052.

O'Brien, S.J., 1998. Geology of the Connaigre Peninsula and adjacent areas, southern Newfoundland. Geological Survey, Department of Mines and Energy, Open File Map NFLD/2660; 1:100 000 scale.

Parra, T., Vidal, O., Agard, P., 2002. A thermodynamic model for Fe-Mg dioctahedral K white micas using data from phase-equilibrium experiments and natural pelitic assemblages. Contributions to Mineralogy and Petrology, 143, 706–732, doi:10.1007/s00410-002-0373-6.

Peternell, M., Hasalova, P., Wilson, C.J.L., Piazolo, S., Schulmann, K., 2010. Evaluating quartz crystallographic preferred orientations and the role of deformation partitioning using EBSD and fabric analyser techniques. Journal of Structural Geology 32, 803–817. doi:10.1016/j.jsg.2010.05.007

Pleuger, J., Mancktelow, N., Zwingmann, H., Manser, M., 2012. K-Ar dating of synkinematic clay gouges from Neoalpine faults of the Central, Western and Eastern Alps. Tectonophysics, 550-553, 1-16, doi:10.1016/j.tecto.2012.05.001.

Renne, P.R., Mundil, R., Balco, G., Min, K., Ludwig, K., 2010. Joint determination of ^{40}K decay constants and $^{40}Ar^*/^{40}K$ for the Fish Canyon sanidine standard, and improved accuracy for $^{40}Ar/^{39}Ar$ geochronology. Geochimica et Cosmochimica Acta 74, 5349-5367.

Reuter, A., Dallmeyer, R. D. (1989). K-Ar and $^{40}Ar/^{39}Ar$ dating of cleavage formed during very low-grade metamorphism: a review. Geological Society, London, Special Publications, 43(1), 161-171.

Schmid, S.M., and Casey, M., 1986. Complete fabric analysis of some commonly observed quartz c-axis patterns, in: Hobbs, B.E., Heard, H.C. (Eds.), Mineral and Rock Deformation Laboratory Studies. American Geophysical Union, pp. 263–286.

Schofield, D.I., D'Lemos, R.S., 1998. Relationships between syn-tectonic granite fabrics and regional PTtd paths: an example from the Gander-Avalon boundary of NE Newfoundland. Journal of Structural Geology, 20, 459-471.

Schofield, D.I., D'Lemos, R.S., 2000. Granite petrogenesis in the Gander Zone, NE Newfoundland: mixing of melts from multiple sources and the role of lithospheric delamination. Canadian Journal of Earth Sciences 37, 535-547.

Sherlock, S.C., Kelley, S.P., Zalasiewicz, J.A., Schofield, D.I., Evans, J.A., Merriman, R.J., Kemp, S.J., 2003. Precise dating of low-temperature deformation: strain-fringe analysis by $^{40}Ar/^{39}Ar$ laser microprobe. Geology, 31, 219-222.

Stipp, M., Stünitz, H., Heilbronner, R., Schmid, S.M., 2002. The eastern Tonale fault zone: a "natural laboratory" for crystal plastic deformation of quartz over a temperature range from 250 to 700 degrees C. Journal of Structural Geology, 24, 1861–1884.

Stockmal, G.S., Colman-Sadd, S.P., Keen, C.E., Marillier, F., O'Brien, S.J., Quinlan, G.M., 1990. Deep seismic structure and plate tectonic evolution of the Canadian Appalachians. Tectonics, 9, 45-62.

Torgersen, E., Viola, G., Zwingmann, H., Henderson, I.C.H., 2015. Inclined illite K-Ar age spectra in brittle fault gouges. Terra Nova, doi: 10.1111/ter.12136

Valverde-Vaquero, P., van Staal, C.R., McNicoll, V., Dunning, G.R., 2006. Mid-Late Ordovician magmatism and metamorphism along the Gander margin in central Newfoundland. Journal of the Geological Society, London, 163, 347-362.

van der Pluijm, B.A., Hall, C.M., Vrolijk, P.J., Pevear, D.R., Covey, M.C., 2001. The dating of shallow faults in the Earth's crust. Nature, 412, 172–175.

van Staal, C.R., 1994. The Brunswick subduction complex in the Canadian Appalachians: record of the Late Ordovician to Late Silurian collision between Laurentia and the Gander margin of Avalon. Tectonics, 13, 946-962.

van Staal, C.R., Barr, S.M., 2012. Lithospheric architecture and tectonic evolution of the Canadian Appalachians and associated Atlantic margin. Tectonic styles in Canada: The LITHOPROBE perspective. Ed. J.A. Percival, F.A. Cool and R.M. Clowes. Geological Association of Canada, Special Paper, 49, 95 p.

van Staal, C.R., Sullivan, R.W., Whalen, J.B., 1996. Provenance and tectonic history of the Gander Margin in the Caledonian/Appalachian Orogen: Implications for the origin and assembly of Avalonia. In: Nance, R.D., and Thompson, M.D. (eds) Avalonian and Related Peri-Gondwanan Terranes of the Circum-North Atlantic. Geological Society of America, Special Paper, 304, 347–367.

van Staal, C.R., Dewey, J.F., Mac Niociall, C., McKerrow, W.S., 1998. The Cambrian-Silurian tectonic evolution of the northern Appalachians and British Caledonides: history of a

complex, west and southwest Pacific-type segment of Iapetus. Geological Society, London, Special Publication, 143, 197-242.

van Staal, C.R., Whalen, J.B., Valverde-Vaquero, P., Zagorevski, A. Rogers, N., 2009. Pre-Carboniferous, episodic accretion-related, orogenesis along the Laurentian margin of the northern Appalachians. In Murphy, J.B., Keppie, J.D. and Hynes, A.J., eds., Ancient Orogens and Modern Analogues. Geological Society, London, Special Publications, 327, 271-316.

van Staal, C.R., Zagorevski, A., McNicoll, V.J., Rogers, N., 2014. Time-transgressive Salinic and Acadian orogenesis, magmatism and Old Red Sandstone sedimentation in Newfoundland. Geoscience Canada, 41, 138-164.

Vidal, O., Parra, T., 2000. Exhumation paths of high pressure metapelites obtained from local equilibria for chlorite-phengite assemblages. Geological Journal, 35, 139–161, doi:10.1002/gj.856.

Viete, D.R., Forster, M.A., Lister, G.S., 2011. The nature and origin of the Barrovian metamorphism, Scotland: $^{40}Ar/^{39}Ar$ apparent age patterns and the duration of metamorphism in the biotite zone. Journal of the Geological Society, 168, 133-146.

Villa, I.M., 2015. ^{39}Ar-^{40}Ar geochronology of mono- and polymetamorphic basement rocks. Periodico di Mineralogia, 84, 615-632.

Villa, I.M., 2016. Diffusion in mineral geochronometers: present and absent. Chemical Geology, 420, 1-10.

Waldron, J.W.F., Barr, S.M., Park, A.F., White, C.E., Hibbard, J., 2015. Late Paleozoic strike-slip faults in Maritime Canada and their role in the reconfiguration of the northern Appalachian orogen. Tectonics, 34, 1661-1684.

Warren, C.J., Smye, A.J., Kelley, S.P., and Sherlock, S.C., 2012a. Using white mica $^{40}Ar/^{39}Ar$ data as a tracer for fluid flow and permeability under high-P conditions: Tauern Window, Eastern Alps. Journal of Metamorphic Geology, 30, 63-80.

Warren, C. J., Hanke, F., Kelley, S. P., 2012b. When can muscovite $^{40}Ar/^{39}Ar$ dating constrain the timing of metamorphic exhumation? Chemical Geology, 291, 79-86.

Wheeler, J., 1996, Diffarg: A program for simulating argon diffusion profiles in minerals: Computers & Geosciences, v. 22, (8), p. 919-929, DOI: 10.1016/S0098-3004(96)00061-1.

Whitney, D.L., and Evans, B.W., 2010. Abbreviations for names of rock-forming minerals. American Mineralogist, 95, 185-187.

Williams I.S., Hergt, J.M., 2000, U-Pb dating of Tasmanian dolerites: a cautionary tale of SHRIMP analyses of high-U zircon. Beyond 2000: New Frontiers in Isotope Geoscience conference, p. 185188.

Willner, A.P., Barr, S.M., Glodny, J., Massonne, H.-J., Sudo, M., Thomson, S.N., van Staal, C.R., White, C., 2015. Effects of fluid flow, cooling and deformation as recorded by $^{40}Ar/^{39}Ar$, Rb-Sr and zircon fission track ages in very low- to low-grade metamorphic rocks in Avalonian SE Cape Breton Island (Nova Scotia, Canada). Geological Magazine, 152, 767-787.

Wilson, C.J.L., Russell-Head, D.S., Kunze, Viola, G., 2007. The analysis of quartz c-axis fabrics using a modified optical microscope. Journal of Microscopy, 227, 30–41.

Zwingmann, H., Mancktelow, N., 2004. Timing of Alpine fault gouges. EPSL, 223, 415-425.

Zwingmann, H., Mancktelow, N., Antognini, M., Lucchini, R., 2010. Dating of shallow faults – new constraints from the AlpTransit tunnel site (Switzerland). Geology, 38, 487-490; doi10.1130/G30785.1

Figures

Figure 1. A. Tectonic domains and extent of deformation of orogenic events for the Appalachian orogen in Eastern Canada, modified from van Staal et al. (2009). Location of Fig. 1B is outlined. B. Geological map of the study area within central-eastern Newfoundland, with sample locations indicated, modified from Hibbard et al. (2006). The Dover and Hermitage Bay faults separate rocks of Ganderian affinity from those of Avalonian affinity. The western extent of sinistral ductile shear attributed to the Wing Pond shear zone and docking of Avalonia against Ganderia is indicated with a dotted red line and follows D'Lemos et al. (1997) in the north, is interpreted for the central portion of the map area, and is undocumented south of the Ackley Granite. Later dextral reactivation along the Dover fault is largely confined to within 1 km of the fault trace, illustrated with the solid red line, and local splays (e.g. Holdsworth, 1994; D'Lemos et al., 1997).

Figure 2. A. Sampling site of VL-12-NF-08, collecting from the central granite dyke, which cross-cuts tightly folded thinly-bedded metapelitic schist and metasandstone. Outcrop height is ~15 m, and view is towards the east. The dyke is oriented parallel to the axial plane of southeasterly overturned F_2 folds. B. Sampling site of 12-KNA-002. The photo is a plan view of the outcrop. NE-striking sinistral S-C' fabric is preserved in mylonitized granite. C. Plan view photograph of dextral shear sense preserved as sigma clasts and S-C' fabric in host Cambrian(?)-Ordovician gneiss at sampling location of 12-KNA-005, Dover Fault. D. Cross-cutting relationship between sample 12-KNA-006 and host gneiss within Dover Fault. Chisel is ~20 cm

in length. E. Schematic cross-section illustrating the structural setting of the samples in this study.

Figure 3. A. Thin section image, crossed polars, and B. back-scattered electron (BSE) image of sample VL-12-NF-08. Inset in A: arrow points to recrystallized tip of white mica grain. C. Thin section image, crossed polars, and D. BSE image of sample 12-KNA-002. E. Thin section image, crossed polars, and F. BSE image of sample 12-KNA-005. Inset in E: arrow points to large muscovite grain exhibiting undulose extinction. G. Thin section image, crossed polars, and H. BSE image of sample 12-KNA-006. Mineral abbreviations follow Whitney and Evans (2010).

Figure 4. Microstructural characteristics and measured quartz c-axis diagrams. All *c*-axis and contour plots are shown as lower hemisphere, equal area projections with a vertical east-west plane defining the orientation of the main foliation in the specimen. The lineation in each specimen occurs as a horizontal east-west line. Contours are drawn at 1% intervals. Fabric skeletons are drawn to outline the interpreted fabric used to constrain fabric opening angles (as shown). For each sample analysed, A) VL-12-NF-08, B) 12-KNA-002, C) 12-KNA-005, and D) 12-KNA-006 a cross-polarized full thin section photo is shown on the left with rectangles indicating the position of more detailed photomicrographs. The numbers in the rectangles correspond to the numbers shown in the photomicrographs for each sample. All photomicrographs are cross polarized with the exception of detailed view 1 for sample VL-12-NF-08 and the right side of the composite detailed photos 1 and 2 of 12-KNA-005, which are plane polarized light. Red arrows in B and D point to sub-grains.

Figure 5. U-Pb results plotted in Concordia diagrams. All data displayed are corrected for common Pb using ^{204}Pb. Data point error ellipses are 2σ. A. VL-12-NF-08 zircon cores. B. VL-12-NF-08 zircon rims, with inset displaying representative analyzed cores and rims, imaged with CL. C. 12-KNA-002 zircon U-Pb results with inset displaying representative zircon grains imaged with BSE (left) and CL (right). D. 12-KNA-005 zircon U-Pb results showing inheritance. E. shows data used to calculate weighted mean ^{206}Pb/^{238}U date, with inset showing zircon grains imaged with BSE (left) and CL (right). F. 12-KNA-005 monazite results, with (G) displaying ^{206}Pb/^{238}U monazite dates compared to the zircon ^{206}Pb/^{238}U crystallization age. Inset shows BSE image of a typical monazite grain with apatite + allanite corona. Weighted mean plots of data are shown in Fig. A6.

Figure 6. White mica step heating results plotted as Ar release spectra for A. VL-12-NF-08, B. 12-KNA-002, C. 12-KNA-005, D. 12-KNA-006. Error bars and results are displayed at the 2σ level. Bold text corresponds to filled boxes. Plateau dates include heating steps delineated by arrows. Statistical details are listed in the text and in the supplementary data. Otherwise, reported dates correspond to integrated dates. Plots were constructed using MassSpec software version 7.93 (Deino, 2001).

Figure 7. A. Reflected light photograph mosaic of disc CA 7-1 from sample VL-12-NF-08 showing *in situ* laser spot locations for ^{40}Ar/^{39}Ar analyses, approximately 5 mm in diameter. Laser spots are circled and labelled as spot_age (Ma). B. Macroscope photograph of disc CA 4-5. C used to guide laser spot analysis. Plot showing distribution of spot ^{40}Ar/^{39}Ar dates with horizontal bars indicating other relevant data: weighted mean zircon ^{206}Pb/^{238}U date of the same

sample (this work), step heat plateau and weighted mean in situ $^{40}Ar/^{39}Ar$ dates from the same sample (this work) and the crystallization age ($^{206}Pb/^{238}U$ zircon) of the post-tectonic Ackley pluton (Fig. 1B; Kellett et al., 2014). D shows date transects for grains F, G and H, with x-axis representing relative distance of data point from left grain edge. A best fit line is shown on Grain F. Errors for $^{40}Ar/^{39}Ar$ *in situ* data do not include error in J as they are plotted here for intra-disc comparison.

Figure 8. A. Reflected light photograph mosaic of disc CA 1-3 from sample 12-KNA-002 showing *in situ* laser spot locations for $^{40}Ar/^{39}Ar$ analyses, approximately 4 mm in vertical dimension. Laser spots are circled and labelled as spot_age (Ma). B. Macroscope photograph of disc CA 1-3 used to guide laser spot analysis. C. Plot showing distribution of spot $^{40}Ar/^{39}Ar$ ages with horizontal bars indicating: weighted mean zircon $^{206}Pb/^{238}U$ age of the same sample (this work), step heat integrated and weighted mean in situ $^{40}Ar/^{39}Ar$ ages from the same sample (this work) and the crystallization age ($^{206}Pb/^{238}U$ zircon) of the post-tectonic Ackley pluton (Fig. 1B; Kellett et al., 2014). Plot constructed with Isoplot 3.71. Errors for $^{40}Ar/^{39}Ar$ *in situ* data do not include error in J as they are plotted here for intra-disc comparison.

Figure 9. A. Reflected light photograph mosaic of disc CA 4-5 from sample 12-KNA-005 showing *in situ* laser spot locations for $^{40}Ar/^{39}Ar$ analyses, approximately 5 mm in vertical dimension. Laser spots are circled and labelled as spot_age (Ma). B. Macroscope photograph of disc CA 4-5 used to guide laser spot analysis. C. Plot showing distribution of spot $^{40}Ar/^{39}Ar$ dates (black) and monazite $^{206}Pb/^{238}U$ dates (grey), with bars indicating other relevant data: weighted mean zircon $^{206}Pb/^{238}U$ dates from the same sample (this work), step heat plateau and weighted

mean in situ $^{40}Ar/^{39}Ar$ dates from the same sample (this work) and the crystallization age ($^{206}Pb/^{238}U$ zircon) of the post-tectonic Ackley pluton (Kellett et al., 2014). Errors for $^{40}Ar/^{39}Ar$ *in situ* data do not include error in J as they are plotted here for intra-disc comparison. Plots constructed with Isoplot 3.71.

Figure 10. Summary of all age-deformation data and tectonic interpretations. For map legend, see Figure 1. *Kellett et al., 2014.

Tables

Table 1. Sample locations, methods applied

Table 2. White mica compositional data

Table 3. *In situ* $^{40}Ar/^{39}Ar$ results

Table 4. Fault gouge clay K-Ar results

Appendix

Sample preparation, characterization and geochronology methodologies for SHRIMP U-Pb, $^{40}Ar/^{39}Ar$ step heating, $^{40}Ar/^{39}Ar$ in situ, and K-Ar analyses.

Figure A1. White mica characterization. Electron microprobe (EMP) compositional data for white mica from samples dated by the in situ $^{40}Ar/^{39}Ar$ method, plotted in an Al_2O_3-FeO+MgO-K_2O ternary diagram. This plot summarizes the intra-sample homogeneity of the white mica summarized in Table 2. See Table A1 for full results and Figures A2-A4 for spot locations of analyses.

Figure A2. BSE and EMP chemical maps (Al, K, Ca, Fe, Si) of white mica in VL-12-NF-08. Labelled grains in the chemical maps correspond to spot analyses in Table A1. Note the lack of zoning in the mapped white mica grains for Al, K, Fe and Si.

Figure A3. BSE and EMP chemical maps (Al, K, Ca, Fe, Si) of white mica in 12-KNA-002. Labelled grains in the chemical maps correspond to spot analyses in Table A1. Note the lack of zoning in the mapped white mica grains for Al, K, Fe and Si.

Figure A4. BSE and EMP chemical maps (Al, K, Ca, Fe, Si) of white mica in 12-KNA-005. Labelled grains in the chemical maps correspond to spot analyses in Table A1. Note the lack of zoning in the mapped white mica grains for Al, K, Fe and Si.

Figure A5. BSE and CL images of zircon and monazite used to guide SHRIMP U-Pb analyses. Images show spot locations corresponding to the analyses in Table A1. 10868 – VL-12-NF-08; 10996 – 12-KNA-002; 10865 – 12-KNA-005. Pages 1-77 are zircon images and pages 78-102 are monazite images.

Figure A6. A-D. Zircon weighted mean $^{206}Pb/^{238}U$ plots, with error bars at 1σ. E. Plot showing U concentration (ppm) vs. SHRIMP ^{204}Pb corrected $^{206}Pb/^{238}U$ date (Ma) for zircon analyzed from sample VL-12-NF-08. Red line at 2500 ppm U indicates cutoff in this study above which there is a clear and erroneous positive correlation between U and date (arrow). Spot analyses with U >

2500 ppm were not used in interpretation of results. Plots were constructed using Isoplot v. 4.15 (Ludwig, 2003).

Figure A7. Inverse isochron plots of white mica step heat $^{40}Ar/^{39}Ar$ data. Consistent with the step heat date spectra plots, only step comprising at least 1% of total ^{39}Ar released are plotted. Step heat aliquot plots were constructed using MassSpec software (Deino, 2001), and in situ plots were constructed using Isoplot v. 4.15 (Ludwig, 2003). Red ellipses were excluded from linear regressions. Error ellipses represent 2σ.

Figure A8. Characterization of fault gouge clay, KNA-013-017. A. Clump of <2 μm clay particles imaged with secondary electrons (SE). B, C show high magnification images of A under BSE and SE, respectively. Arrows indicate fibrous clay grains, and black dot shows location of EDS spectrum displayed in H. D. Clump of <2 μm clay particles imaged with BSE. E, F show high magnification images of D under BSE and SE, respectively. Arrows indicate fibrous clay grains, and black dot shows location of EDS spectrum displayed in I. G. X-ray diffractogram of KNA-013-017 fault gouge clay used to determine semi-quantitative composition. See analytical details for smear, glycol and heat tests in the supplementary data. H. Electron dispersive spectrometer (EDS) spectrum of spot indicated in C. I. EDS spectrum of spot indicated in F. Note that the clay clumps were sitting on a carbon surface to limit charging in the scanning electron microscope, resulting in large C peaks in the EDS spectra.

Table A1. White mica electron microprobe compositional data.

Table A2. Full SHRIMP U-Pb results.

Table A3. Full $^{40}Ar/^{39}Ar$ step heating results.

Table A4. Full *In situ* $^{40}Ar/^{39}Ar$ results including blank analyses.

Figure 1

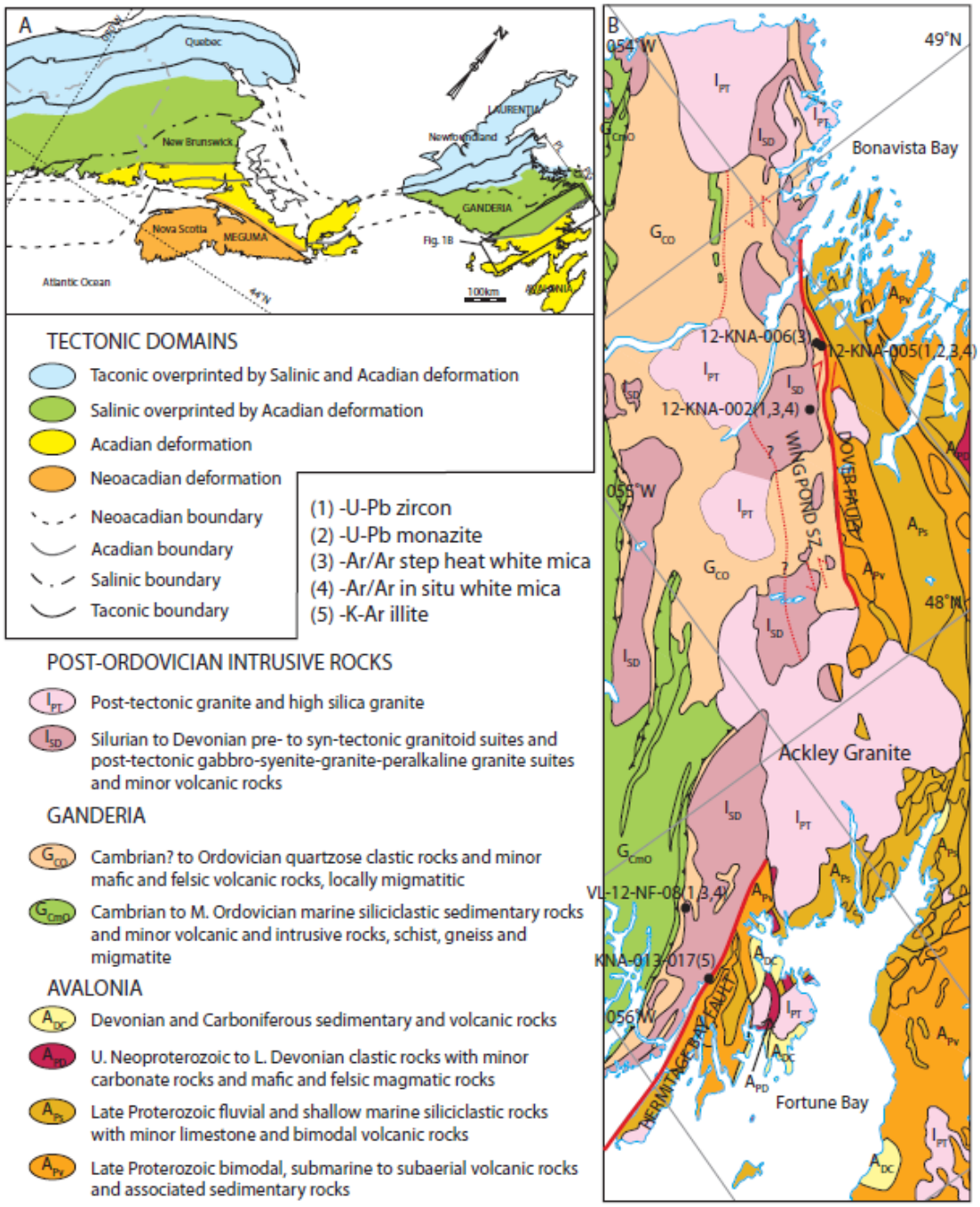

Figure 2

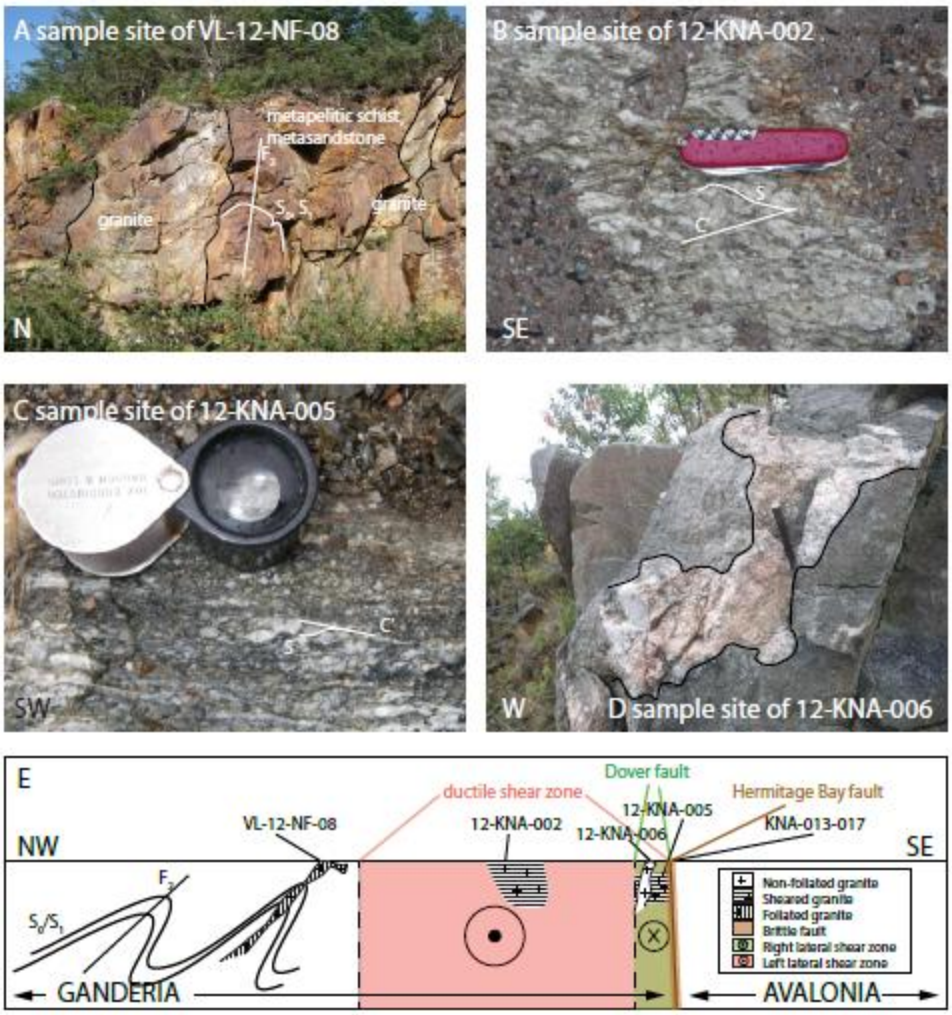

Figure 3

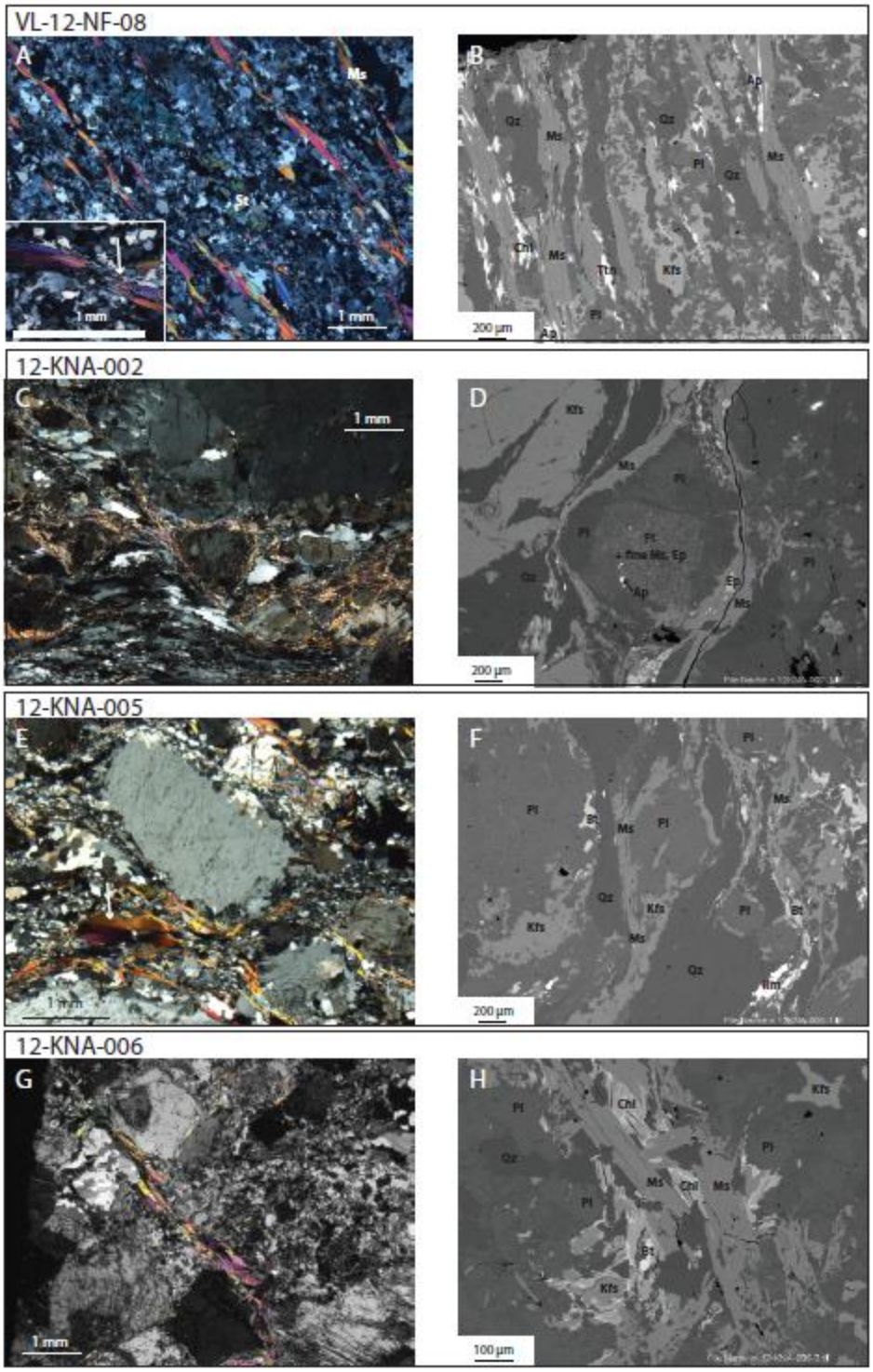

Figure 4

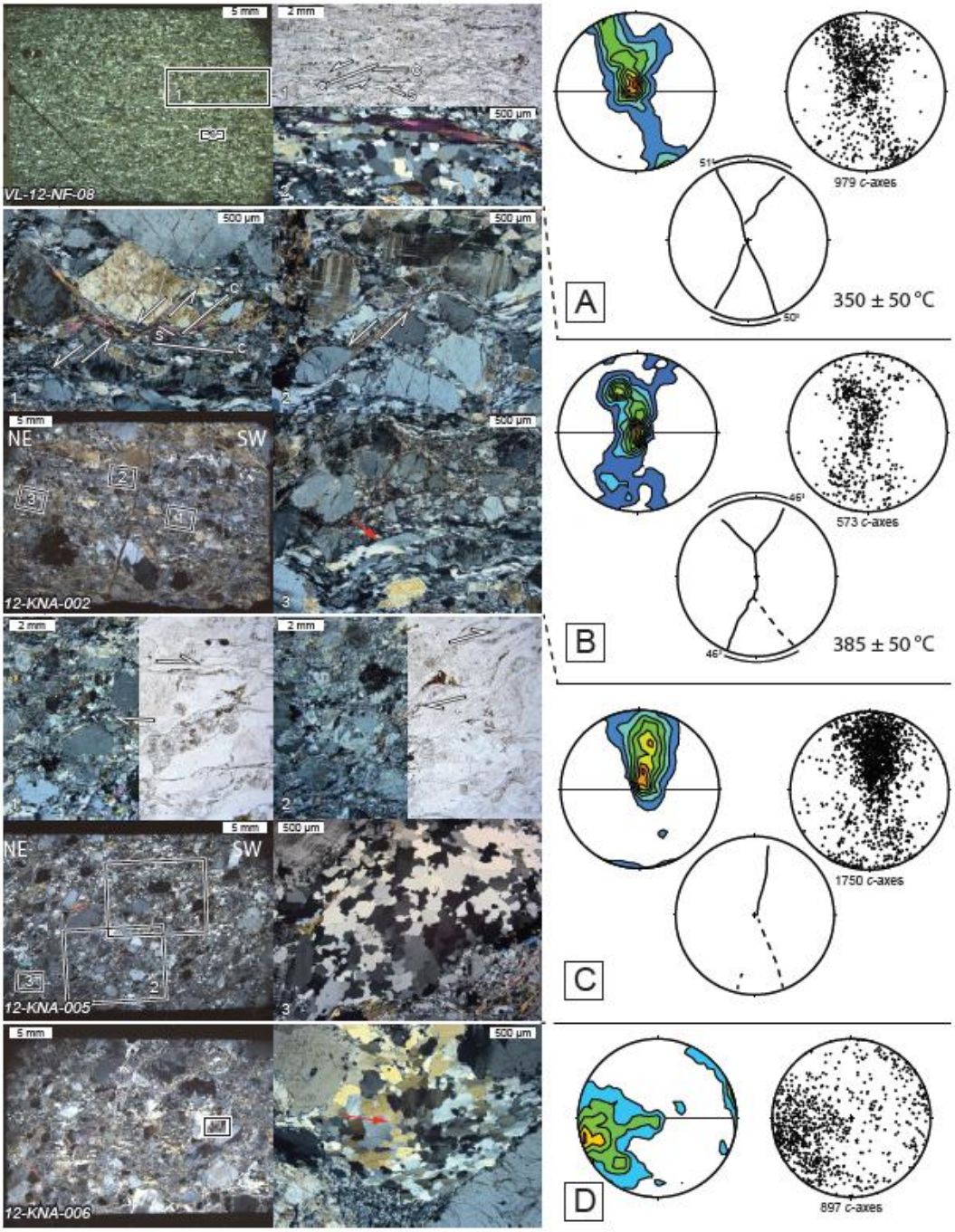

Figure 5

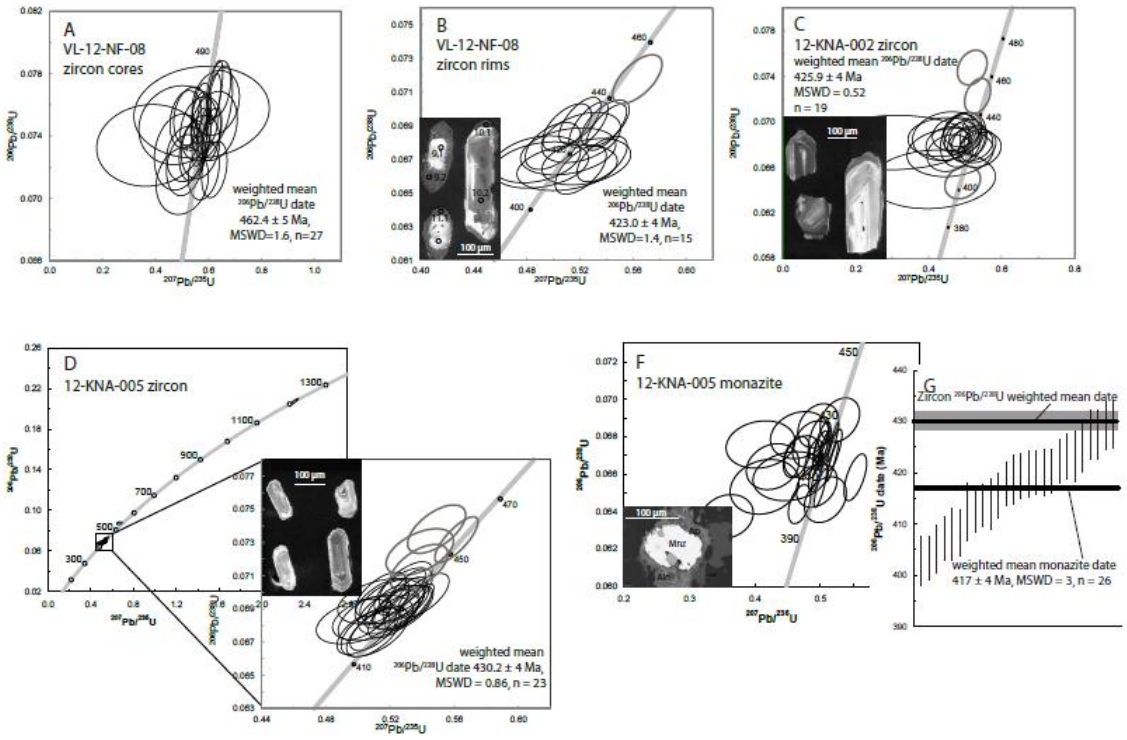

Figure 6

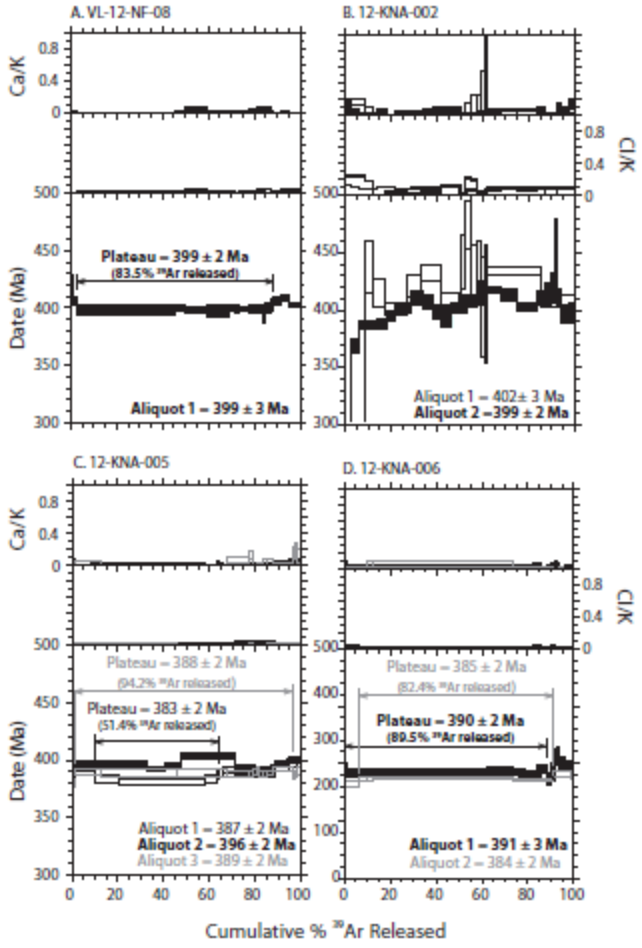

Figure 7

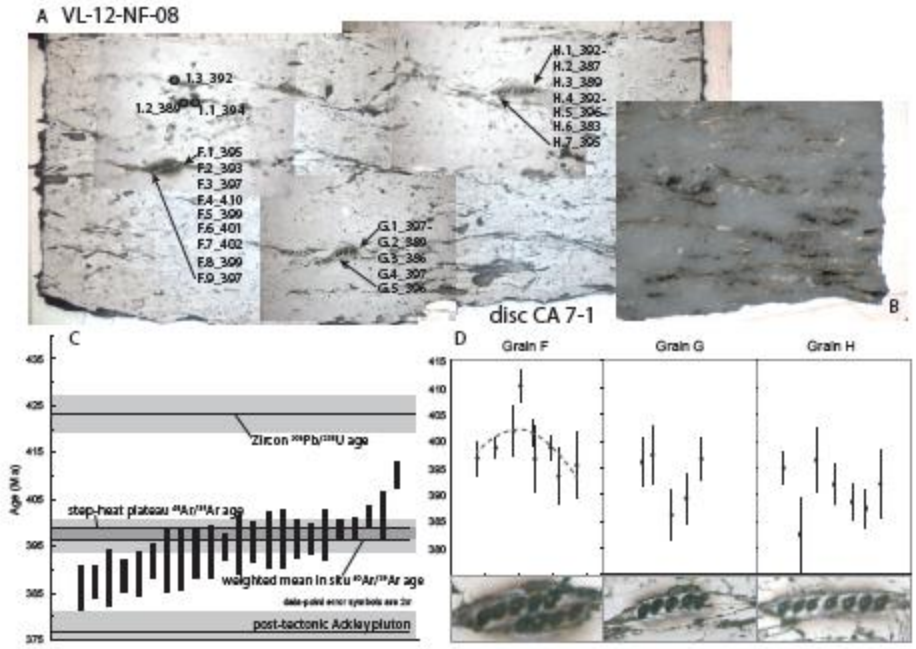

Figure 8

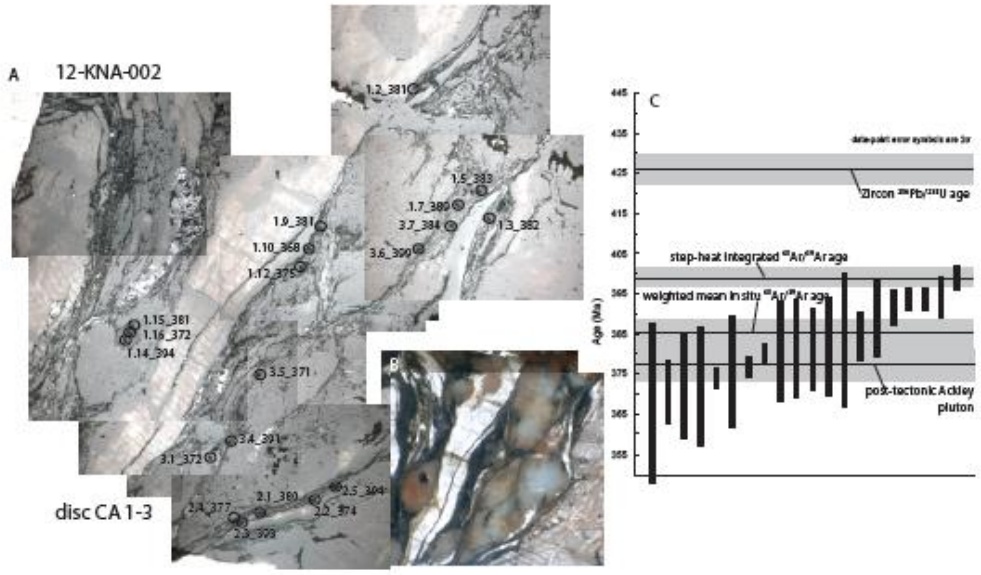

Figure 9

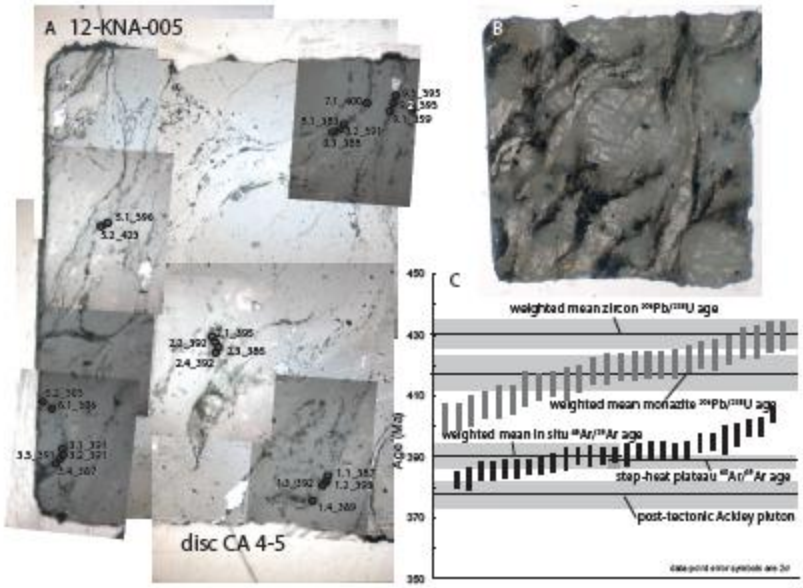

Figure 10

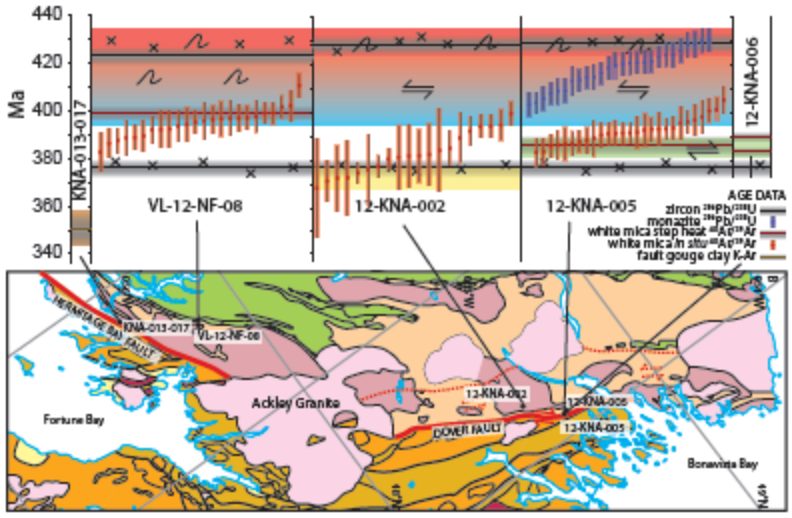

430-423 Ma - widespread syn-tectonic magmatism, peak metamorphic conditions during Salinic orogeny.

ca. 423-395 Ma - Wing Pond sinistral shear zone and regional retrograde metamorphism during Acadian orogeny. Docking of Avalonia.

ca. 384 Ma - Dover fault dextral shear zone, reactivated during Neoacadian orogeny. Docking of Meguma.

ca. 377 Ma - Post-tectonic Ackley pluton stitches Dover fault, local hydrothermal circulation.*

≤ ca. 351 Ma - Brittle slip on Hermitage Bay fault, latest Neoacadian orogeny.

Table 1. Sample locations (NAD83), methods applied and summary of results. (c)-core, (r)-rim. *integrated age, no plateau age obtained.

Sample name	Shear sense	Deformation T (±50 ºC)	Lat (ºN)	Long (ºW)	Zircon U-Pb (Ma)	Monazite U-Pb (Ma)	White mica $^{40}Ar/^{39}Ar$ plateau (Ma)	White mica $^{40}Ar/^{39}Ar$ in situ mean (Ma)	K/Ar (Ma)
VL-12-NF-08	Only localized	385 ºC	47.81806	055.58639	462.4±5(c), 423±4(r)		399±2	396.6±2.5	
12-KNA-002	Left lateral	350 ºC	48.54567	054.22635	425.9±4		399±2*, 402±3*	385±4	
12-KNA-005	Right lateral		48.68150	054.10512	430±4	417±4	388±2, 383±2	392±2	
12-KNA-006			48.68760	054.10849			390±2; 385±2		
KNA-013-017			47.67119	055.66555					350.6±7

Table 2. White mica compositional data obtained by electron microprobe wave-dispersive spectroscopy. VL-12-NF-08 results are based on 30 analyses, 12-KNA-002 results on 47 analyses, and 12-KNA-005 results on 31 analyses. Full results are available in the supplementary data. FeO* represents total Fe. Calculations based on Vidal and Parra (2000) and Parra et al. (2002).

	VL-12-NF-08				**12-KNA-002**				**12-KNA-005**			
	Min	**Mean**	**Max**	**Std**	**Min**	**Mean**	**Max**	**Std**	**Min**	**Mean**	**Max**	**Std**
SiO_2	45.72	46.82	53.52	1.34	44.33	47.86	50.96	1.24	45.27	46.80	48.37	0.88
TiO_2	0.38	0.51	0.67	0.07	0.07	0.35	1.08	0.24	0.38	0.99	1.63	0.24
Al_2O_3	28.94	33.27	34.27	1.06	24.58	28.54	30.87	1.25	27.74	29.77	31.04	0.79
FeO*	1.56	1.89	4.94	0.63	4.49	5.87	12.13	1.32	4.70	5.29	5.93	0.24
MnO	0.00	0.02	0.12	0.02	0.02	0.06	0.22	0.03	0.00	0.03	0.06	0.02
MgO	0.47	0.67	1.36	0.18	1.29	1.83	5.72	0.67	0.68	1.11	1.55	0.28
CaO	0.00	0.01	0.05	0.01	0.00	0.02	0.24	0.04	0.00	0.03	0.39	0.09
Na_2O	0.21	0.40	0.54	0.07	0.11	0.17	0.44	0.05	0.14	0.28	0.40	0.07
K_2O	9.25	10.79	11.11	0.36	7.23	10.71	11.18	0.64	10.43	10.89	11.09	0.15
Total	***93.50***	***94.38***	***95.21***	*0.46*	***91.67***	***95.43***	***97.37***	*1.12*	***93.68***	***95.20***	***97.39***	*0.84*
Si	3.111	3.158	3.516	0.071	3.105	3.262	3.453	0.054	3.127	3.196	3.268	0.040
Ti	0.019	0.026	0.034	0.004	0.003	0.018	0.056	0.013	0.019	0.051	0.084	0.012
Al	2.241	2.645	2.716	0.091	2.029	2.291	2.407	0.081	2.243	2.396	2.506	0.068
Fe	0.088	0.107	0.283	0.036	0.253	0.335	0.710	0.079	0.270	0.302	0.335	0.014
Mn	0.000	0.001	0.007	0.001	0.001	0.003	0.013	0.002	0.000	0.002	0.003	0.001
Mg	0.047	0.067	0.139	0.018	0.131	0.186	0.597	0.071	0.070	0.113	0.157	0.028
Ca	0.000	0.000	0.003	0.001	0.000	0.002	0.018	0.003	0.000	0.002	0.029	0.006
Na	0.028	0.053	0.070	0.010	0.014	0.023	0.058	0.007	0.019	0.037	0.053	0.009
K	0.775	0.928	0.952	0.033	0.646	0.931	0.976	0.051	0.918	0.949	0.970	0.012
Musc	***68%***	***87%***	***90%***	***4%***	***46%***	***72%***	***78%***	***5%***	***71%***	***76%***	***78%***	***2%***
Parag	***2%***	***5%***	***7%***	***1%***	***1%***	***2%***	***3%***	***1%***	***1%***	***3%***	***4%***	***1%***

Fe-Celad	***6%***	***7%***	***15%***	***2%***	***19%***	***25%***	***45%***	***4%***	***18%***	***20%***	***26%***	***2%***
Pyroph	***0%***	***1%***	***13%***	***2%***	***0%***	***2%***	***8%***	***1%***	***0%***	***0%***	***1%***	***0%***

Table 3. *In situ* $^{40}Ar/^{39}Ar$ results.

Spot	^{40}Ar	+/-	^{39}Ar	+/-	^{38}Ar		^{37}Ar	+/-	^{36}Ar	+/-	$^{40}Ar^*/^{39}Ar$	+/-	**Age_{uncorr}	+/-	+/- (no J error)	$Age_{atmcorr}$	+/-	+/-(no J error)	Preferred age (Ma)	+/-	+/-(no J error)
***12-KNA-002, disc CA 1-3,* J = 0.00964 ± 0.0000964**																					
1_1	7194	111	276.6	4.6	3.4	0.7	13.8	5.2	1.2	1.7	26.0	0.6	404.2	9.0	8.2	385.7	27.4	27.2			
1_2	19257	114	763.6	6.5	9.0	0.8	98.1	5.2	2.1	1.7	25.2	0.3	393.1	5.1	3.7	**381.2**	**10.7**	**10.1**	**381.2**	**10.7**	**10.1**
1_3	16131	114	629.4	6.2	9.9	1.2	72.8	5.2	2.5	1.7	25.6	0.3	398.8	5.7	4.4	**381.7**	**12.6**	**12.2**	**381.7**	**12.6**	**12.2**
1_4	3097	111	114.8	3.8	3.9	0.9	10.0	5.2	2.0	1.7	27.0	1.3	417.7	18.7	18.3	343.4	66.8	66.7			
1_5	12414	113	461.7	5.8	5.8	0.8	25.9	5.2	3.6	1.7	26.9	0.4	416.3	6.9	5.7	**383.4**	**16.9**	**16.5**	**383.4**	**16.9**	**16.5**
1_6	9307	113	339.3	5.1	4.6	0.7	34.4	5.2	4.4	1.7	27.4	0.5	423.9	8.2	7.3	369.5	22.8	22.5			
1_7	21975	115	836.9	7.5	11.5	1.2	32.0	5.2	3.8	1.7	26.3	0.3	407.6	5.3	3.8	**388.6**	**9.9**	**9.3**	**388.6**	**9.9**	**9.3**
1_8	1294	111	48.2	3.5	0.8	0.7	8.5	5.2	0.9	1.7	26.9	3.0	415.9	42.0	41.7	337.5	157.5	157.5			
1_9	16124	114	637.9	7.1	7.2	0.8	50.8	5.2	1.9	1.7	25.3	0.3	393.9	5.8	4.6	**381.1**	**12.7**	**12.2**	**381.1**	**12.7**	**12.2**
1_10	10126	113	383.5	5.2	4.2	0.7	113.9	5.2	3.8	1.7	26.4	0.5	409.6	7.4	6.4	**367.8**	**20.2**	**19.9**	**367.8**	**20.2**	**19.9**
1_11	9654	113	352.3	5.1	4.0	0.7	23.7	5.2	3.0	1.7	27.4	0.5	423.5	8.0	7.0	388.0	21.7	21.5			
1_12	15676	114	558.2	6.2	6.5	0.7	90.9	5.2	7.7	1.7	28.1	0.4	432.8	6.4	5.1	**375.4**	**14.2**	**13.8**	**375.4**	**14.2**	**13.8**
1_13	3357	112	127.5	4.0	0.9	0.6	-0.2	5.2	1.1	1.7	26.3	1.2	408.5	17.1	16.7	371.1	59.2	59.1			
1_14	13271	112	524.9	6.1	6.2	0.8	21.5	5.2	-0.4	1.9	25.3	0.4	**394.0**	**6.2**	**5.1**	396.7	15.8	15.4	**394.0**	**6.2**	**5.1**
1_15	16542	114	623.5	6.5	7.8	0.7	36.7	5.2	4.6	1.7	26.5	0.3	411.4	5.9	4.6	**380.6**	**12.9**	**12.4**	**380.6**	**12.9**	**12.4**
1_16	13425	113	523.7	6.1	7.9	1.1	72.5	5.2	3.3	1.7	25.6	0.4	398.9	6.3	5.2	**372.1**	**15.1**	**14.7**	**372.1**	**15.1**	**14.7**

2_1	44128	46	1689.6	10.3	19.0	0.8	312.2	9.7	10.4	0.5	26.1	0.2	405.6	4.3	2.2	**379.8**	**4.2**	**2.5**	**379.8**	**4.2**	**2.5**
2_2	32225	105	1284.3	7.0	18.3	1.5	1008.9	8.4	5.2	0.3	25.1	0.2	391.3	4.2	2.2	**374.1**	**4.2**	**2.5**	**374.1**	**4.2**	**2.5**
2_3	26766	104	1060.4	7.2	11.8	0.6	263.9	8.4	0.4	0.6	25.2	0.2	**393.4**	**4.5**	**2.8**	391.4	5.1	3.7	**393.4**	**4.5**	**2.8**
2_4	31540	103	1250.6	7.7	13.5	0.7	681.5	8.4	4.8	0.3	25.2	0.2	393.1	4.3	2.5	**376.8**	**4.3**	**2.6**	**376.8**	**4.3**	**2.6**
2_5	26523	104	1050.4	7.5	8.6	1.0	96.9	8.4	0.0	1.0	25.3	0.2	**393.5**	**4.6**	**2.9**	393.1	6.0	4.9	**393.5**	**4.6**	**2.9**
3_1	12034	119	438.9	5.1	8.6	1.0	57.9	10.5	5.5	1.2	27.4	0.4	423.7	6.9	5.7	**371.9**	**13.3**	**12.9**	**371.9**	**13.3**	**12.9**
3_2	8906	116	270.2	4.2	7.2	1.1	67.5	10.5	10.3	1.2	33.0	0.7	498.6	9.9	8.8	342.9	21.1	20.8			
3_4	15803	119	629.6	6.0	6.6	0.5	15.1	10.5	-0.4	1.3	25.1	0.3	**391.4**	**5.5**	**4.3**	393.8	10.3	9.7	**391.4**	**5.5**	**4.3**
3_5	18180	120	731.4	5.8	8.1	0.5	1.6	10.5	3.0	1.2	24.9	0.3	388.0	5.0	3.6	**370.7**	**8.5**	**7.8**	**370.7**	**8.5**	**7.8**
3_6	25510	121	995.6	7.0	13.5	1.3	0.8	10.5	-0.5	1.3	25.6	0.2	**398.7**	**4.7**	**3.0**	400.4	7.2	6.3	**398.7**	**4.7**	**3.0**
3_7	25275	121	952.6	6.8	11.6	0.6	6.0	10.5	6.2	1.2	26.5	0.2	411.4	4.9	3.1	**384.3**	**7.0**	**6.1**	**384.3**	**7.0**	**6.1**
12-KNA-005, disc CA 4-5, J = 0.00962 ± 0.0000962																					
1_1	26576	74	1070.8	8.2	13.2	1.5	-1.1	6.7	1.3	1.2	24.8	0.2	386.5	4.5	2.8	381.0	6.6	2.8	386.5	4.5	2.8
1_2	28231	72	1117.1	7.7	12.0	0.9	-4.6	6.7	-1.7	1.4	25.3	0.2	392.9	4.4	2.6	398.5	6.7	2.6	392.9	4.4	2.6
1_3	29684	76	1176.2	9.1	16.6	1.8	-14.7	6.7	0.2	1.5	25.2	0.2	392.4	4.6	2.9	391.2	7.0	2.9	392.4	4.6	2.9
1_4	23275	72	906.8	7.2	15.2	1.5	-11.9	6.8	2.1	1.2	25.7	0.2	398.4	4.7	3.0	388.6	7.3	3.0	388.6	7.3	3.0
2_1	29598	77	1069.2	7.9	16.5	1.5	0.7	6.8	8.1	1.3	27.7	0.2	426.3	4.8	3.0	394.9	6.7	3.0	394.9	6.7	3.0
2_2	27827	74	1065.2	7.8	14.4	1.6	12.9	6.8	3.2	1.2	26.1	0.2	404.7	4.6	2.8	392.0	6.6	2.8	392.0	6.6	2.8
2_3	27893	73	1102.0	8.5	11.5	0.9	12.5	6.8	1.8	1.2	25.3	0.2	393.4	4.6	2.9	386.2	6.5	2.9	386.2	6.5	2.9
2_4	29170	78	1122.3	7.9	12.2	0.9	8.4	6.8	2.7	1.3	26.0	0.2	402.9	4.5	2.7	392.4	6.4	2.7	392.4	6.4	2.7
3_1	30790	75	1226.4	8.6	12.5	0.9	4.8	6.8	-1.5	1.4	25.1	0.2	390.5	4.4	2.6	395.1	6.4	2.6	390.5	4.4	2.6
3_2	30617	74	1218.6	7.6	12.4	0.9	1.6	6.8	1.0	1.2	25.1	0.2	390.8	4.2	2.3	387.1	5.9	2.3	390.8	4.2	2.3

3_3	30212	76	1202.7	8.1	16.1	1.4	5.1	6.8	-2.5	1.4	25.1	0.2	390.7	4.3	2.5	398.9	6.5	2.5	390.7	4.3	2.5
3_4	36725	79	1476.6	9.1	14.7	0.9	14.5	6.8	-0.7	1.4	24.9	0.2	387.2	4.2	2.3	388.7	5.7	2.3	387.2	4.2	2.3
4_1	17852	70	712.1	6.7	7.0	0.8	16.2	6.8	0.0	1.2	25.1	0.3	390.0	5.0	3.6	389.7	8.8	3.6	390.0	5.0	3.6
4_2	22452	73	894.1	7.9	8.9	0.9	21.9	6.8	0.8	1.2	25.1	0.2	390.6	4.8	3.3	386.4	7.5	3.3	390.6	4.8	3.3
5_1	13598	69	533.1	6.6	5.5	0.8	56.7	6.8	-1.8	1.4	25.5	0.3	396.2	5.9	4.8	409.2	12.3	4.8	396.2	5.9	4.8
5_2	15161	71	533.8	6.2	5.4	0.9	49.2	6.8	1.6	1.2	28.4	0.4	436.1	6.2	4.9	423.2	11.2	4.9	423.2	11.2	4.9
6_1	26709	73	1078.9	8.2	11.3	0.9	13.0	6.8	-1.9	1.4	24.8	0.2	385.6	4.5	2.8	392.6	7.0	2.8	385.6	4.5	2.8
6_2	17635	71	717.6	7.0	7.9	0.9	11.2	6.8	0.9	1.2	24.6	0.3	383.1	5.0	3.7	377.4	8.8	3.7	383.1	5.0	3.7
7_1	18954	49	734.2	6.2	7.1	0.5	16.9	1.8	-0.9	1.1	25.8	0.2	400.4	4.8	3.2	405.2	7.9	3.2	400.4	4.8	3.2
8_1	28241	52	1111.2	9.2	11.5	0.6	13.2	1.8	3.1	0.9	25.4	0.2	394.8	4.7	3.0	382.8	5.6	3.0	382.8	5.6	3.0
8_2	24860	55	879.9	7.3	11.9	1.1	47.1	1.8	9.2	0.9	28.3	0.2	434.1	5.1	3.3	391.1	6.4	3.3	391.1	6.4	3.3
8_3	34251	91	1326.3	9.2	14.2	0.6	-10.8	8.1	4.0	0.7	25.8	0.2	400.6	4.5	2.7	387.7	4.9	2.7	387.7	4.9	2.7
9_1	28015	90	1177.9	8.1	12.5	0.6	76.1	8.1	3.7	0.7	23.8	0.2	371.9	4.2	2.5	358.5	4.8	2.5	358.5	4.8	2.5
9_2	40206	93	1592.2	9.4	16.4	0.7	-3.0	8.1	0.7	0.9	25.3	0.2	392.6	4.2	2.2	390.4	4.8	2.2	392.6	4.2	2.2
9_3	33286	93	1307.9	9.3	14.3	0.7	19.7	8.1	0.7	0.9	25.5	0.2	395.4	4.5	2.7	392.8	5.3	2.7	395.4	4.5	2.7
10_1	34489	91	1308.3	8.3	13.5	0.7	-4.3	8.1	1.0	0.9	26.4	0.2	408.0	4.4	2.5	404.4	5.3	2.5	404.4	5.3	2.5
10_2	21243	88	815.6	7.4	11.0	1.1	-8.6	8.1	1.1	0.9	26.0	0.3	403.6	5.1	3.6	397.4	6.7	3.6	397.4	6.7	3.6
10_3	35955	95	1394.7	10.3	16.4	0.7	0.3	8.1	0.7	0.9	25.8	0.2	399.9	4.6	2.8	397.4	5.3	2.8	399.9	4.6	2.8
10_4	23366	89	888.0	7.0	8.6	0.5	68.7	8.1	4.5	0.7	26.3	0.2	407.4	4.9	3.2	385.9	5.8	3.2	385.9	5.8	3.2
VL-12-NF-08, disc CA 7-1, J = 0.00969 ± 0.0000969																					
1_1	18322	248	728.5	5.7	8.1	0.5	1.6	2.7	0.7	0.7	25.2	0.4	394.0	6.6	5.5	389.9	7.6	6.7	394.0	6.6	5.5
1_2	17171	248	693.6	6.5	7.9	0.6	15.1	2.7	0.3	0.7	24.8	0.4	388.5	7.0	6.0	386.0	8.1	7.3	388.5	7.0	6.0

1_3	21683	249	846.3	7.8	9.3	0.7	4.6	2.7	1.6	0.7	25.6	0.4	400.6	6.4	5.3	392.2	7.2	6.3	392.2	7.2	6.3
F-1	20948	56	813.5	7.5	8.1	1.0	-28.3	32.5	1.3	1.0	25.8	0.2	402.5	5.0	3.4	395.4	7.2	6.3	395.4	7.2	6.3
F-2	28129	58	1026.3	8.4	12.0	1.0	9.2	32.5	7.9	1.0	27.4	0.2	425.6	5.0	3.2	393.4	6.2	5.1	393.4	6.2	5.1
F-3	32180	100	1270.1	21.3	11.9	1.0	-17.2	32.5	-1.1	1.2	25.3	0.4	396.6	7.0	6.1	399.8	8.0	7.2	396.6	7.0	6.1
F-4	28489	60	1082.8	8.1	11.0	1.0	10.2	32.5	0.0	1.2	26.3	0.2	410.3	4.7	2.8	409.7	6.4	5.3	410.3	4.7	2.8
F-5	44368	65	1740.7	10.5	17.8	1.3	45.1	32.6	0.0	1.2	25.5	0.2	398.8	4.2	2.2	398.4	5.1	3.6	398.8	4.2	2.2
F-6	44022	61	1714.8	11.4	19.4	2.0	-38.9	32.6	-2.2	1.2	25.7	0.2	401.4	4.4	2.4	406.3	5.3	3.9	401.4	4.4	2.4
F-7	48573	119	1862.0	21.3	20.2	1.1	-12.5	32.6	2.2	1.0	26.1	0.3	407.2	5.6	4.3	401.8	6.0	4.8	401.8	6.0	4.8
F-8	40558	62	1591.6	8.4	20.8	1.7	-29.1	32.6	0.9	1.0	25.5	0.1	398.7	4.1	2.0	395.8	4.9	3.3	398.7	4.1	2.0
F-9	44573	66	1709.7	9.2	23.1	1.7	-27.1	32.6	4.0	1.0	26.1	0.1	407.0	4.2	2.0	396.8	4.8	3.2	396.8	4.8	3.2
H-1	25809	58	800.9	7.5	12.1	1.0	2.3	32.7	19.5	1.1	32.2	0.3	491.1	6.0	4.2	391.9	7.4	6.5	391.9	7.4	6.5
H-2	40688	60	1589.8	9.9	17.6	1.1	213.7	32.7	4.7	1.0	25.6	0.2	400.3	4.3	2.3	387.4	4.9	3.5	387.4	4.9	3.5
H-3	41833	65	1614.1	9.3	21.9	1.5	101.1	32.7	6.1	1.0	25.9	0.2	404.8	4.2	2.2	388.6	4.9	3.4	388.6	4.9	3.4
H-4	42541	67	1526.3	9.9	20.4	1.6	98.5	32.7	14.7	1.1	27.9	0.2	432.0	4.6	2.6	391.9	5.1	3.7	391.9	5.1	3.7
H-5	31572	82	1013.4	7.6	16.6	1.4	7.6	5.8	19.9	1.3	31.2	0.2	476.8	5.4	3.3	396.4	7.0	6.0	396.4	7.0	6.0
H-6	23931	78	864.5	7.3	10.3	0.6	17.2	5.8	9.7	1.3	27.7	0.3	429.4	5.2	3.5	382.5	7.7	6.9	382.5	7.7	6.9
H-7	25529	78	1012.4	7.6	11.5	0.6	31.3	5.8	0.8	1.4	25.2	0.2	395.0	4.6	2.9	391.1	7.3	6.4	395.0	4.6	2.9
G-1	49386	85	1591.1	9.2	21.6	0.7	17.5	5.8	30.5	1.3	31.0	0.2	475.2	4.9	2.5	396.7	5.4	4.1	396.7	5.4	4.1
G-2	34281	84	1299.3	8.5	13.7	0.7	10.7	5.8	6.8	1.3	26.4	0.2	411.3	4.5	2.6	389.3	5.9	4.7	389.3	5.9	4.7
G-3	34206	83	1344.6	8.7	16.8	1.7	0.6	5.8	3.7	1.3	25.4	0.2	398.1	4.3	2.5	386.2	5.8	4.6	386.2	5.8	4.6
G-4	32960	82	1258.9	8.1	13.9	0.6	11.3	5.8	3.2	1.4	26.2	0.2	408.5	4.4	2.5	397.4	6.4	5.3	397.4	6.4	5.3
G-5	37904	83	1502.2	9.3	19.3	1.6	4.3	5.8	-0.5	1.4	25.2	0.2	395.2	4.3	2.3	396.0	5.7	4.4	396.0	5.7	4.4

Notes:

Dark grey rows contain analyses for which ^{40}Ar <2x measured blank, and age is considered unreliable.

Decay constants are from Min et al. (2000).
**Age_{uncorr} is uncorrected for atmospheric Ar, see text for details.
Bold text and pale grey boxes indicate ages used for interpretation, see text for details.

HIGHLIGHTS

6. Low temperature deformation and fluid events redistribute ^{40}Ar in white mica.
7. Dating the timing of deformation recorded by white mica requires *in situ* analysis.
8. Salinic D_2 deformation in Newfoundland Ganderia occurred ca. 422 Ma.
9. Sinistral slip at Ganderia-Avalonia boundary between 422-405 Ma, dextral reactivation ca. 385 Ma.
10. Brittle slip persisted until at least Mississippian.